Canadian Science Publishing | Canadian Journal of Earth Sciences

Origin and paleoenvironmental reconstruction of phosphorus–bearing sandstones of the Cambrian Xinji Formation, southwestern margin of Ordos Basin, China

Journal:	*Canadian Journal of Earth Sciences*
Manuscript ID	cjes-2019-0087.R2
Manuscript Type:	Article
Date Submitted by the Author:	08-Jan-2020
Complete List of Authors:	Liang, Jiwei; Chang'an University, School of Earth Sciences and Resources Tao, Wenxing; Chang'an University, School of Earth Sciences and Resources Ma, Xiaojun; Chang'an University, School of Earth Sciences and Resources
Keyword:	Geochemistry, Paleoenvironment, Phosphorus-bearing sandstones, Xinji Formation, Ordos Basin
Is the invited manuscript for consideration in a Special Issue? :	Not applicable (regular submission)

1 **Origin and paleoenvironmental reconstruction of phosphorus–bearing sandstones of**
2 **the Cambrian Xinji Formation, southwestern margin of Ordos Basin, China**

3 Jiwei Liang*, Wenxing Tao*, Xiaojun Ma
4 School of Earth Sciences and Resources, Chang'an University, Xi'an 710054, China
5

*Corresponding author: Jiwei Liang (email: jiweil@chd.edu.cn).

Wenxing Tao (email: twx9571@126.com).

Abstract: Increasing exploration interest in oil and gas hosted by early Cambrian strata has focused research effort on early Cambrian sandstones. The origin of phosphorus and the paleoenvironment of phosphorus-bearing sandstones from the Xinji Formation are discussed in this paper. X-ray diffraction, optical microscopy, grain size analysis, total organic carbon (TOC), and the concentrations of major, trace, and rare earth elements (REEs) are analyzed in this work. The sandstones are mostly sublitharenite, with calcareous cement. The quartz content of the sandstone samples is 39.8–73.9%, with illite (7.9–27.6%) and calcite (4.5–29%). The mineral particles of sandstone samples are mainly well sorted with fine particle size, suggesting strong paleohydrodynamic force. The value of SiO_2 is 37.69–78.19%, followed by Al_2O_3 (6.11–13.67%). Compared with UCC, the boron of sandstone samples is relatively enriched, while Sc, Sr, and Ba are relatively depleted. The ΣREE content is 124.46–323.99 ppm. Phosphorus is biogenic origin and enriched by upwelling current. The source of the Xinji Formation sandstone samples was mainly a mixture of sedimentary rock, granite and alkali basalt, with the provenance of terrestrial clastic materials. The sandstone deposited under oxic condition and warm and humid paleoclimate with saline to brackish feature in the passive continental margin. Phosphorus occurred in sandstones is sensitive to paleoclimate that can be used as an indicator to judged paleoclimate, and is more enriched in warm and humid weather.

Key words: Geochemistry; Paleoenvironment; Phosphorus-bearing sandstones; Xinji Formation; Ordos Basin

1. Introduction

The Ordos Basin is the largest petroliferous basin in China (Zhang et al. 2000; Hou et al. 2003; Xi et al. 2006; Liu et al. 2009; Shi et al. 2009). Current oil and gas exploration effort in the basin is focused on tight upper Paleozoic sandstones and Ordovician carbonate rocks (Zhang et al. 2000; Hou et al. 2003; Xi et al. 2006; Liu et al. 2009; Shi et al. 2009). There are few studies of the lower Paleozoic sandstones because these stratums are deeply buried and drilling data are sparse. However, increasing exploration interest has drawn attention to the lower Paleozoic sandstones. Previous studies have shown that the Xinji Formation sandstone is thick with superior reservoir physical properties, showing favorable hydrocarbon exploration potential (Chen 2011; Li et al. 2012; Liu 2015). Regional geological surveys have shown that sedimentation of the Xinji Formation was accompanied by transgression in the southwest margin of the Ordos Basin (Zhang 1981; Li et al. 2012; Chen et al. 2012). Previous studies indicate that the sandstone from Xinji Formation contains high phosphorus (Feng et al. 1989; Zhu et al. 2008; Chen et al. 2012; Chen et al. 2013; Bai et al. 2018) and the studies on phosphorus-bearing sandstone have focused on the petrography and paleobiology. The sedimentary evolution of early Cambrian has been studied by lithological association, sedimentary cycle, and paleontological fossil form numerous profiles in North China, show that Xinji Formation is significant layer for mine of sedimentary phosphate and typical clastic rocks with high content phosphorus (Zhu et al. 2008). For discussing the time of basal Xinji Formation, the trace fossils has been researched through sections in Norh China, indicates that bottom of Xinji Foration not earlier than Canglangpu Stage possibly (Miao et al. 2014). The *Microdictyon* paltes from the lower Xinji Formation along southern North China were discovered for the first time and analyzed characteristics (Pan et al. 2017). According to recently research result, the microbially induced sedimentary structures (MISS) is associated with sedimentary

environment, which raises the view about Xinji Formation in Henan province is tidal-flat face (Bai et al. 2018). The origin of the phosphorus and the paleoenvironment of these sandstones have not been investigated till now. Geochemistry can be used to place semi-quantitative and quantitative constraints on the paleoenvironment (Vincent et al. 2006; Yan et al. 2007; Zhang 2008), which affects the enrichment of phosphorus in sandstone.

In this paper, data from X-ray diffraction, optical microscopy, grain size analysis and the concentrations of major, trace, and rare earth elements (REEs) are combined with analyses of the total organic carbon content of the Xinji Formation phosphorus-bearing sandstones from a profile at Jingfushan, Longxian, Baoji City. The petrological and geochemical characteristics are analyzed, and the origin of the phosphorus and the paleoenvironment are discussed. The results can provide valuable insights for oil and gas exploration in the lower Paleozoic sandstones in the south-western margin of the Ordos Basin.

2. Geological Settings

The Ordos Basin is part of the North China Plate, and overlies the cratonic basement of the North China Block. Continental rifting in the Ordos area occurred as a consequence of the Jinning orogeny (Li 1999; Chen et al. 2013). Rifting ceased at the end of the Jinning orogeny, and the basin underwent craton depression and marginal subsidence. The South China Plate collided with the North China Plate during the Indo-China period; this collision produced the Qinling orogenic belt and uplifted the southern area (Li and Li 2008; Deng et al. 2013; Li et al. 2017). The present-day tectonic and geomorphologic features of the Ordos Basin formed during the Yanshanian to Himalayan periods (Li and Li 2008; Deng et al. 2013; Li et al. 2017). Transgression began in the southwest during the Cambrian, with sedimentation of barrier-free shoreface deposits, including clastic deposition of

phosphorus-bearing sandstones (Feng et al. 1989; Chen et al. 2013; Liu 2015; Wang 2018). From bottom to top, units in the study area are the Luoquan Formation, the Xinji Formation, the Zhushadong Formation, the Mantou Formation, the Maozhuang Formation, the Xuzhuang Formation, the Zhangxia Formation, and the Sanshanzi Formation (Wang 2018). The southwest lower contact of the Xinji Formation is a parallel unconformity with the underlying Sinian Luoquan Formation. The upper contact is conformable with the Zhushadong Formation. The Xinji Formation in Ordos Basin was mainly distributed in Longxian and Qishan, with the thickness decreasing from west to east, and there is no deposit in the east margin of basin (Zhu et al. 2008; Chen et al. 2012). The Xinji Formation contains alternating layers of thinly bedded phosphate-bearing argillaceous siltite, siltite, argillaceous fine sandstone, and fine sandstone, interbedded with dolostone (Chen et al. 2012; Bai et al. 2018).

The Shuiyan village is located in Longxian, Baoji City, Ordos Basin (Fig. 1), where the deposition of Xinji Formation is characterized by phosphorus-bearing clastic rocks. Here, sandstones of the Xinji Formation have well-defined top and bottom boundaries and clear outcrops. The sandstone is intercalated with dolomite and thin mudstone (Fig. 2).

3. Samples and Methods

Twenty-five sandstone samples were collected from the Xinji Formation sandstone profile (Fig. 2). In all of these samples, the concentrations of major elements, trace elements and rare earth elements were analyzed. X-ray diffraction was performed on eleven sandstone samples. Thirteen sandstone samples were cut into slices for grain size analysis and nine sandstones optical microscopy. Eight argillaceous sandstone samples were analyzed for total organic carbon (TOC). All samples were kept in sealed bags prior to analysis to prevent contamination.

For TOC analysis, argillaceous sandstones samples were ground to a powder of less

than 200mesh, and the inorganic carbon in the sample was removed with HCl. Organic carbon was converted to CO_2 and measured with a Multi EA2000. The test method followed GB/T 194145-2003. The analysis was carried out in the Key Laboratory of Oil and Gas Resource Exploration Technology at Yangtze University, China.

All sandstone samples for major element analysis were ground to 200mesh. The major elements were measured using AA-6800 atomic absorption spectrometry, UV-2600 UV-visible spectrometry, and by X-ray fluorescence spectrometry. The analysis process follows that of GB/T14506.1~14-2010 and Yandokan et al. (2015). Uncertainties on the analyses are less than 1%.

Sandstone samples for trace element and rare earth element analysis were ground to 200mesh and dissolved in $HF+HNO_3$ mixtures in Teflon bombs at 190^{o}C for 48 hours. Element concentrations were determined by ICP–MS using a Perkin–Elmer Sciex Elan 6000. The analysis procedure follows that of GB/T14506.30-2010. Uncertainties on the analyses are less than 1%.

Minerals contents of sandstone samples were identified by X-ray diffraction on a D8 ADVANCE powder diffractometer. The analysis process complies with the oil and gas industry standard SY/T 6210-1996; Uncertainties are within 5%.

Sandstone samples for grain size analysis were cut into slices and processed according to gas industry standard SY/T 5913-2004. Images used to perform the grain size analysis were obtained on a ZEISS Axio Scope A1 polarizing microscope equipped with a CIAS-2004 digital color image analysis system. Operation of the equipment followed the standard SY/T 5434-2009.

4. Results

4.1 Petrological and mineralogical analysis

The contract relation of minerals was point and line contact, and grain size were fine

with good sorting and poor rounding under microscopy. Quartz was the principal mineral identified using optical microscopy with high carbonate cement and low feldspar minerals content (Fig. 3), and biodetritus was found in some samples (Fig. 3(a)–(b)). By estimating relative mineral content, the sandstone samples are classified as sublitharenite (Table 1 and Fig. 4(a)). It is worth noting that glauconite was observed under the microscope (Fig. 3(c)–(f)), and the some minerals were corroded in samples, included quartz and mica (Fig. 3(d)–(e)). Mica was corroded turn to hydromica, which exhibits some degree of preferred orientation (Fig. 3(d)–(e)).

Quartz takes the main proportion in sandstone samples (39.8–73.9%, average = 59.18%). Furthermore, the content of illite (7.9–27.6%, average = 16.35%), calcite (4.5–29%, average = 12.66%), and feldspar (7.5–17%, average = 10.84%) is relatively high, with minor abundance of chlorite (0.1–2.3%, average = 0.98%), anhydrite (0.8–1.3%, average = 0.96%), and hematite (0.2–2.8%, average = 1.27%) (Table 2).

4.2 Grain size analysis

Grain size analysis can reflect the intensity of hydrodynamic forces during deposition (Folk and Ward 1957; Johnson 2010; Seward and Hails 2010). The range of average particle size (M_Z) of the sandstone samples is 3.89–4.46Φ (average 4.1Φ) (Table 3), with the majority of the samples falling in the range of 3.9–4.3Φ. Larger values of M_Z indicate smaller particle sizes (Folk and Ward 1957; Johnson 2010; Seward and Hails 2010). So, particle sizes of sandstones in Xinji Formation are mostly small. Typically, the sandstone grain-size decreases through units, from macro-grained at the bottom to fine-grained at the top.

The standard deviation (σ_1) represents sediment separation condition, and the σ_1 values of >4.00, 2.00–4.00, 1.00–2.00, 0.71–1.00, 0.50–0.71, 0.35–0.50, and <0.35 are associated with the sorting of very poor, generally poor, poor, medium, generally good, good, and very

good, respectively. Furthermore, smaller values of σ_1 show better sorting and thus stronger hydrodynamic forces (Folk and Ward 1957; Johnson 2010; Seward and Hails 2010). The value of σ_1 of the samples was between 0.30 and 0.52, with an average of 0.42 (Table 3), indicating that the sorting is good and hydrodynamic forces could be vigorous.

The skewness (SK_1) suggests the skew direction of the peak of the frequency curve (Folk and Ward 1957; Johnson 2010; Seward and Hails 2010). SK_1 values of -1.0– -3.0, -3.0– -0.1, -0.1–0.1, 0.1–0.3, and 0.3–1.0 suggest very negatively skewed, negatively skewed, symmetrical, positively skewed, and very positively skewed respectively. The positive curve indicates that the sediments are mostly large-grained components, while the negative curve shows that the sediments are mainly fine-grained components (Folk and Ward 1957; Johnson 2010; Seward and Hails 2010). The value of SK_1 of the samples was ranged from -0.69 to 0.24 (average −0.13) (Table 3), reflecting that the grain-size curves are mostly negatively skewed and the abundance of fine-grained components.

The kurtosis (K_G) can reflect the sharpness of the grain size frequency curve (Folk and Ward 1957; Johnson 2010; Seward and Hails 2010). Value of K_G of <0.67, 0.67−0.90, 0.90−1.11, 1.11−1.56, 1.56−3.00, and >3.00 indicates very flat, flat, medium, sharp, very sharp, and acute sharp (Folk and Ward 1957; Johnson 2010; Seward and Hails 2010). The sample K_G ranges in 1.45–2.91 (average 1.76), showing relatively strong sharpness.

4.3 Geochemical analysis

4.3.1 TOC and major elements

The TOC content of the argillaceous sandstones ranges in 0.06–0.63% with an average of 0.29% (Table 4). The SiO_2 contents (37.69–78.19%, average = 61.59%) and Al_2O_3 contents (6.11–13.67%, average = 9.16%) of the sandstone samples are relatively high, while the rest element abundance is relatively low (<5%) (Table 4). Compared to the Upper Continental Crust (UCC), P_2O_5 and CaO are obviously enriched (Fig. 5).

177 4.3.2 Trace elements

178 The elements Zr, Th, B, Hf, and Y are enriched relative to the UCC, while Co, Sc, Sr,
179 Ba, and U are depleted (Table 6). The enrichment or depletion of the trace elements was
180 evaluated quantitatively using the enrichment factor (EF) (McLennan 2001; Li et al. 2017),
181 defined by EF = $(X_{sample}/Al_{sample})/(X_{UCC}/Al_{UCC})$, where X is the trace element (ppm). After
182 calculating EF, the trace elements in the sandstone samples were divided into three groups
183 (Table 7). Boron was the only element in Group 1, with an average EF ≥ 5. Co, Zr, Th, U,
184 Hf, and Y fell in Group 2, with an average EF ranges from 1 to 5 (1 ≤ average EF ≤ 5), and
185 Sc, Sr, and Ba were included in Group 3, with an average EF < 1 (Fig. 6(a)).

186 4.3.3 Rare earth elements

187 The total ΣREE concentration in the sandstone samples was 124.46–323.99 ppm with
188 an average of 205.85 ppm (Table 9). The average ΣREE concentration is slightly higher
189 than that of the UCC (146 ppm). Compared with chondrite (Table 8), the light rare earth
190 elements (LREEs) show more enriched pattern than heavy rare earth elements (HREEs)
191 (Fig. 6(b)).

192 REEs might be associated with fine-grained minerals and organic matter (Boynton
193 1984; Hou 2010; Li et al. 2017), generally. The negative correlation between ΣREE and
194 SiO_2 (r = -0.47) suggests that REEs possibly not occur in fine-grained minerals such as clay
195 minerals (Fig. 7(a)). Furthermore, ΣREE shows a positive correlation with P_2O_5 (r = 0.43)
196 and TOC (r = 0.55) (Fig. 7(b)–(c)). TOC and phosphorus are two indicators to organic
197 matter (Wang 1989; Wang et al. 2016; Li et al. 2017). Thus, the REEs mostly coexist with
198 organic matter.

199 The values of L/H, $(La/Yb)_N$, $(La/Sm)_N$, and $(Gd/Yb)_N$ can record enrichment or
200 depletion between the LREEs and HREEs (Elderfield and Greaves 1982; Bo et al. 2007).
201 High values of L/H and $(La/Yb)_N > 1$ can reflect the enrichment of LREEs while low L/H

202 and $(La/Yb)_N$ < 1 show depletion. Values of $(La/Sm)_N$ and $(Gd/Yb)_N$ reflect the
203 fractionation of LREEs and HREEs, and the higher values indicate stronger fractionation
204 degrees (Hoyle et al. 1984; Ling et al. 2006). The values of L/H $(La/Yb)_N$, $(La/Sm)_N$ and
205 $(Gd/Yb)_N$ of sandstone samples range in 5.05–10.57 (average = 7.50) , 2.72–10.66 (average
206 = 7.14), 1.18–4.30 (average = 3.35), and 1.32–1.83 (average = 1.52) (Table 9). All these
207 values indicate that the LREEs are relatively higher fractionated than the HREEs.

208 **5. Discussion**

209 5.1 Petrography and Geochemistry characteristics

210 Quartz corroded and hydromica orientated in some samples (Fig. 3(d)–(e)), which is
211 indicative of extensive diagenesis. Generally, the glauconite can be reflected
212 paleoenvironment (Ordin and Matter, 1981; Kitamura, 1998). According to the previous
213 studies, the glauconite from ancient stratum can be associated with transgression, reflecting
214 that shallow water and strong hydrodynamic force (Chafetz and Reid, 2000; Xu et al.
215 2010). The glauconite in the samples indicate marine sedimentation environment under
216 transgression and shallow water with high-energy hydrodynamic force. All the above
217 petrography characteristics are in accordance with the results of mineralogical and grain
218 size analyses.

219 Triangulation chart of the relative proportions of CaO, SiO_2, and Al_2O_3 can reflect the
220 mineral component of sedimentary rock (Li et al. 2017). The SiO_2 is the most abundant
221 element in Xinji Formation sandstone samples, so ternary diagram shows that quartz is
222 mostly mineral present (Fig. 4(b)), which is also accorded with XRD results.

223 5.2 Origin of phosphorus

224 Previous studies indicate that phosphorus in sandstones normally stems from two main
225 sources: biogenic and terrestrial clastic material (Shemesh et al. 1983; Schenau et al. 2000;

226 Xu et al. 2014). The TOC is a measure of the organic matter in argillaceous sandstone, and
227 can be used to recognize biogenic phosphorus (Kennedy et al. 2002; Li et al. 2019). It is
228 worth noting that there is a positive correlation between the phosphorus content of
229 argillaceous sandstone samples and the TOC content (r = 0.57), which indicates that the
230 phosphorus is biogenic (Fig. 8(a)). The Al content can be used to detect the input of
231 terrestrial clastic material (Dai et al. 2011; Wang et al. 2016; Wang et al. 2017). The
232 observed negative correlation between P_2O_5 and Al_2O_3 (r = -0.35) (Fig. 8(b)) suggests that
233 the phosphorus was not provided by terrestrial clastic material, which is in accordance with
234 the biogenic origin inferred from the TOC–P_2O_5 relationship.

235 Previous studies have shown that phosphogenesis is mainly due to the formation of
236 upwelling current (Cook and Shrgold 1984; Wallin 1989; Tamburini et al. 2003). The
237 upwelling current carries phosphorus and nutrients, leading to the proliferation of
238 organisms and the enrichment of phosphorus in the current. Under the action of
239 transgression, phosphorus-bearing sediments were deposited in continental margin zone,
240 forming the phosphorus-bearing sediments (Fig. 9). All the above statements concluded
241 that the phosphorus in the sandstone is mainly biogenic.

242 5.3 Reconstruction of Paleoenvironment

243 5.3.1 Site of deposition and provenance

244 Because the geochemical properties of rare earth elements and some trace elements are
245 stable, and their characteristics are not easy to change when the sediments suffer geological
246 process (Fu et al. 2010; Xu et al. 2014). So the site of deposition and provenance can be
247 estimated through the characterization of these elements (Fu et al. 2011; Wang et al. 2016).
248 The provenance characteristics and types can be evaluated through the diagrams of La/Th–
249 Hf and La/Yb–ΣREE (Floyd and Leveridge 1987; Allègre and Minster 1978). Most
250 sandstone samples of Xinji Formation are located in passive continental margin (Fig.

10(a)), and the source rock types are mixture of sedimentary rock, granite and alkali basalt (Fig. 10(b)). The three-phase diagrams of Th–Sc–La and Co–Th–Zr/10 can be used to identify the tectonic background (Bhatia and Crook 1986; Bauluz et al. 2000). Most of the samples are located in passive margin (PM) (Fig. 11), which is consistence with previous observation. The value of Y/Ho has been used to record the source of clastic material in sediments (Webb and Kamber 1991). The Y/Ho value in terrestrial clastic rocks is about 28, while the Y/Ho value in marine chemical sediments is 44–74 (Bau and Dulski 1996; Xu et al. 2014). The Y/Ho ratio of sandstone samples ranges from 24.69 to 28.47, with an average of 26.76 (Table 5). These values suggest the provenance comes from terrestrial clastic materials.

In a word, all these analyses demonstrate that the sandstone from the Xinji Formation deposited in a passive continental margin and provenance is mixture of sedimentary rock, granite and alkali basalt, with the origin of terrestrial clastic materials.

5.3.2 Paleoclimate

The paleoclimate can be identified through value of MgO/CaO and the increasing ratio corresponds to more hot and dry paleoclimate (Lerman 1979; Xu et al. 2011; Tian et al. 2014). According to previous studies, the MgO/CaO values of sandstones from Shihezi Formation in eastern Ordos Basin are ranged from 0.97 to 5.34 (average = 2.85), indicating that the paleoclimate is hot and dry (Guo et al. 2016). Contrastively, the average MgO/CaO of Guadalupian from Permian in the Penglaitan Section of Laibin, Guangxi province, is about 0.2, reflecting that the paleoclimate is mainly warm and humid (Yang et al. 2009). Similarly, the MgO/CaO ratio of the Xinji Formation sandstone samples ranges in 0.03–0.8 (average = 0.23) (Table 5), suggesting that the paleoclimate varies greatly and was dominated by warm and humid weather.

Referring to the global climate curve, there was a climeate change trend from cold to

warm in the Cambrian period. It means that the Cambrian paleoclimate is mainly warm and humid (Fig. 12). The above result of using geochemical method to restore the paleoclimate of Xinji Formation is consistent with the global climatic characteristics of Cambrian period.

There is an obvious negative correlation between MgO/CaO and P_2O_5 (r = -0.48) (Fig. 13(a)), and TOC (r = -0.61) (Fig. 13(b)). This observation suggests that phosphorus was relatively deficient while the paleoclimate made the transition from warm and humid to hot and dry, and became more enriched when the paleoclimate was warm and humid (Fig. 13(a)). In addition, TOC content decreases with paleoclimate variation from warm and humid to hot and dry (Fig. 13(b)). These phenomena is probably because the warm and humid climate is more favorable for high biological productivity, and then produce more OM while hot and dry climate on the contrary (Schenau et al. 2000; Li et al. 2014). The transgression indicates that the phosphorus-bearing sediments appeared in the warming period of the earth, and the change of climate and sea level played an important role in the phosphorus-bearing sandstone deposit (Wallin 1989; Scheau et al. 2000; Mou et al. 2005). In summarize, warm and humid climate is favorable for the formation of phosphorus-bearing sandstone.

5.3.3 Redox condition

The elements U and Th are redox-sensitive, and ratios such as U/Th and δU (δU = 2U/(U + Th/3)) have been verified to reflect the redox state of an environment (Jones and Manning 1994; Kimura and Watanabe 2001; Tribovillard et al. 2006). Values of U/Th < 0.75 are associated with oxic conditions while U/Th > 1.25 records reducing conditions (Jones and Manning 1994; Kimura and Watanabe 2001; Tribovillard et al. 2006). Values of U/Th for the Xinji Formation sandstone samples are between 0.11 and 0.22 with an average of 0.13 (Table 5), showing an oxic environment. Values of δU < 1 indicate oxic conditions and δU > 1 indicates reducing conditions (Jones and Manning 1994; Kimura and Watanabe

2001; Tribovillard et al. 2006). Values of δU for the sandstone samples are between 0.48 and 0.81 with an average of 0.56 (Table 5). These values are consistent with oxic conditions. Thus, the sandstone samples from the Xinji Formation deposited in an oxic environment.

As mentioned above, the glauconite can indicate the paleoenvironment such as redox conditions. In the modern ocean environment, the glaucontie was usually reflected the deep water and reducing conditions (Amorosi 1995; Xu et al. 2010). But recent researches state that the glaucontie in Proterozoic and Paleozoic was associated with shallow water and oxic conditions (Bamerjee et al. 2016; Tang et al. 2016). This shows that the glaucontie in Xinji Formation shows the oxic conditions. The above results are also consistent with judging consequence of geochemical parameters (U/Th and δU).

5.3.4 Paleosalinity

Generally, boron in solution is absorbed by clay minerals, because it can easily enter into the crystal lattice of clay minerals and would not be desorbed due to the decrease of concentration (Couch 1971; Teng et al. 2005; Li et al. 2017). Therefore, boron can be used as a record of the paleosalinity of the water during sedimentation (Couch 1971; Teng et al. 2005; Li et al. 2017). The paleosalinity was evaluated using formula (1) for Equivalent Boron (Walker 1968),

$$\text{Equivalent Boron} = (11.8 \times T \times 8.5)/(\text{K} \times 1.70 \times (11.8\text{-K})) \quad (1)$$

where T is the concentration of boron (ppm), and K is the K_2O content (%). The criteria proposed by Walker for normal seawater, brackish water, and saline water are 300–400 ppm, 200–300 ppm, and <200 ppm, respectively. The value of Equivalent Boron for the Xinji Formation sandstone samples ranges from 93.46 to 369.86 ppm with an average of 202.54 ppm (Table 5) (Fig. 14). These results correspond to saline to brackish water. The transition to saline conditions may be associated with the initiation of transgression during

326 the Xinji Formation.

327 It is also possible to calculate paleosalinity from Equivalent Boron using the formula
328 (2) (Adams et al. 1965),

329 $$Sp=0.0977\ x - 7.043 \qquad (2)$$

330 where Sp is paleosalinity (‰) and x is Equivalent Boron (ppm). Paleosalinities of 0–
331 0.5‰, 0.5–5‰, 5–18‰, 18–40‰, and >40‰ indicate fresh, saline, brackish, salt, and
332 ultra-salt waters, respectively (Adams et al. 1965; Chang et al. 2009; Li et al. 2019). The Sp
333 value of the samples ranges from 2.09‰ to 29.09‰ with an average of 12.75‰ (Table 5).
334 These values suggest that the Xinji Formation sandstone was deposited in saline to brackish
335 water.

336 The Sr/Ba ratio can also be used to reconstruct paleosalinity (Adachi et al. 2014; Zhao
337 et al. 2016). Values of Sr/Ba > 1, 0.6–1, and <0.6 correspond to seawater, brackish water,
338 and saline water, respectively (Adachi et al. 2014; Zhao et al. 2016). The Sr/Ba ratio of the
339 samples ranges from 0.12 to 1.12 with an average of 0.37 (Table 5), indicating that the
340 Xinji Formation sandstone mainly formed in saline to brackish water, with an increase in
341 salinity towards sea water.

342 **6. Conclusions**

343 This paper scientifically studies the origin of phosphorus-bearing sandstone,
344 paleoenrionment and relationship between phosphorus and paleoenvironment from
345 sandstone profile of the Xinji Formation in the southwestern Ordos Basin. The geological
346 explanations about petrology and geochemistry are discussed in detail. The conclusions
347 obtained are as follows:

348 (1) The optical microscopy and XRD results show that quartz takes the main
349 proportion in sandstone samples and the rock type is sublitharenite. Notably, the glauconite
350 was observed under the microscope, reflecting a marine sedimentary environment and

shallow water with oxic condition. The grain size analyses show that the sandstone samples are mainly well-sorted with finer components, showing strong paleohydrodynamic force.

(2) The positive correlation between P_2O_5 and TOC and the negative correlation between P_2O_5 and Al_2O_3 indicate that the phosphorus is mainly biogenic instead of terrestrial clastic material. Meanwhile, upwelling current and transgression bring the phosphorus and organic matter might be mainly reasons of phosphorus-bearing sediments.

(3) The provenance of Xinji Formation sandstone samples formed from mixture of sedimentary rock, granite and alkali basalt, with the source of terrestrial clastic materials. Geochemical characteristics suggest that the sandstones deposited under oxic condition and warm and humid paleoclimate with saline to brackish feature in the passive continental margin.

(4) The phosphorus content in the Xinji Formation sandstone samples shows a negative correlation with MgO/CaO, reflecting that the relatively warm and humid climate facilitated phosphorus enrichment.

Acknowledgments:

We are grateful to Graeme Brown provided help for the grammar and syntax of paper. We also intend to thank the financial support from the China Geological Survey (No. 0716 – 1641DK900365/07), National Science and Technology Major Project (No. 2017ZX05005002 – 004), and National Natural Science Foundation of China (No. 4150210).

References

Adachi, N., Ezaki, Y., and Liu, J.B. 2014. The Late Early Cambrian microbial reefs immediately after the demise of Archaeoyathan reefs, Hunan province, South China. Palaeogeography, Palaeoclimatology, Palaeoecology, **407**: 45-55.

Adams, T.D., Haynes, J.R., and Walker, C.T. 1965. Boron in Holocene illites of the dovey estuary. Wales, and its relationship to paleosalinity in cyclothems. Sedimentology, **4**(3): 189-195.

Allègre, C.J., and Minster, J.F. 1978. Quantitative models of trace element behavior in

magmatic processes. Earth and Planetary Science Letters, **38**(1): 1-25.
Amorosi, A. 1995. Glaucony and sequence stratigraphy: a conceptual framework of distribution in siliclastic sequences. Journal of Sedimentary Research, **65**: 419-425.
Bai, W.B., Qi, Y.A., Guo, Y.H., Wang, M., and Qing, G.S. 2018. Storm deposits and relevant trace fossils from the Cambrian Series 2 Xinji Formation in Lushan area, Henan Province. Journal of Palaeogeography, **20**(03): 365-376. [in Chinese]
Banerjee, S., Bansal, U., and Thorat, A.V. 2016. A review on paleogeographic implications and temporal variation in glaucony composition. Journal of Paleogeography, **5**: 43-71.
Bau, M., and Dulski, P. 1996. Distribution of yttrium and rare-earth elements in the Penge and Kuruman in-formations, Transvall Supergroup, South Africa. Precambrian Research, **79**(1-2): 37-55.
Bauluz, B., Mayayo, M.J., Fernandez, N.C., and Lopez, J.M. 2000. Geochemistry of Precambrian and Paleozoic siliciclastic rocks from the Iberian Range (NE Spain): Implications for source-area weathering, sorting,provenance,and tectonic setting. Chemical Geology, **168**(1/2): 135-150.
Bhatia, M.R., and Crook, K.A. 1986. Trace element characteristics of graywackes and tectonic setting discrimination of sedimentary basins. Contributions to Mineralogy and Petrology, **92**: 181-193.
Bo, D.Y., Zhou, L., Wang, X.H.,Z hang, X.Y., and Ma, T.Q. 2007. Geochemistry of Nanhuan—Cambrian Sandstones in Southeastern Hunan, and Its Constraints on Neoproterozoic—Early Paleozoic Tectonic Setting of South China. Acta Geologica Sinica, **81**(06): 755-771.
Boynton, W.V. 1984. Chapter 3-Cosmochemistry of the rare earth elements: Meteorite Studies. Developments in Geochemistry, **02**: 63-114.
Chafetz, H.Z., and Reid, A. 2000. Syndepositional shallow-water precipitation of glauconitic minerals. Sedimentary Geology, **136**: 29-42.
Chang, H.J., Zhu, X.L., Feng, L.J., Huang, J., and Zhang, Q.R. 2009. Redox Sensitive Trace Elements as Paleoenvironments Proxies. Geological Review, **55**(1): 91-99.
Chen, A.Q. 2010. Basin evolution and sediments accumulation during Eopaleozoic in Ordos continental block. Ph.D. thesis, Chengdu University of Technology, Chengdu, China. [in Chinese]
Chen, C.Y. 1983. Evolution of geological features of Sinian-Cambrian phosphorite rocks in north China. Mineral Deposits, **04**: 80-90. [in Chinese]
Chen, Q. 2011. Research on the Lithofacies Paleogeography of the Lower Paleozoic in the Southwestern Margin of Ordos. Ph.D. thesis, Northwest university, Xi'an, China. [in Chinese]
Chen, Q.L., Bai, Y.L., Huang, Y., Ma, Y.H., Liu, X.G., Wei, L.H., and et al. 2012. Sequence lithofacies palaeogeography of the Cambrian in Ordos Basin,China. Acta Petrolei Sinica, **33**: 82-94.
Chen, Q.L., Bai, Y.L., Ma, Y.H., and Liu, X.G. 2013. Further Study on Lithofacies Palaeogeography and Sedimentary-Tectonic Evolution of Cambrian in Ordos Basin, North China. Journal of Jilin University (Earth Science Edition), **43**(06): 1697-1715. [in Chinese]
Cook, P.J., and Shergold, J.H. 1984, Phosphorus, phosphorites and skeletal evolution at the Precambrian-Cambiran boundary. Nature, **308**(5956): 231-236.
Couch, E.L. 1971. Calculation of paleosalinites from boron and clay mineral data. AAPG Bulletin, **55**: 1829-1837.
Dai, S.F., Wang, X.B., Zhou, Y.P., Hower, J.C., Li, D.H., Chen, W.M., and et al. 2011. Chemical and mineralogical compositions of silicic, mafic, and alkali tonsteins in the late Permian coals from the Songzao Coalfield, Chongqing, Southwest China.

Chemical Geology, **282**(1-2): 0-44.
Deng, X.Q., Luo, A.X., Zhang, Y., and Liu, X. 2013. Geochronological Comparison on Indosinian Tectonic Events Between Qinling Orogeny and Ordos Basin. Acta Sedimentologica Sinica, **31**: 939-953.
Elderfield, H., and Greaves, M. 1982. The rare earth elements in sea water. Nature, **296**: 214-219.
Feng, Z.Z., Chen, J., and Wu, S. 1989. Lithofacies Paleogeography of Early Paleozoic of North China Platfrom. Journal of Sedimentary, **04**: 16-55. [in Chinese]
Floyd, P.A., and Leveridge, B.E. 1987. Tectonic environment of the Devonian Gramscatho Basin,South Cornwall: Framework mode and geochemical evidence from Turbiditic sandstones. Journal of Geology Society London, **144**(4): 531-542.
Folk, R.L., and Ward, W.C. 1957. Brazos River bar [Texas]; a study in the significance of grain size parameters. Journal of Sedimentary Research, **27**(1): 3-26.
Fu, X.G., Wang, J., Zeng, Y.H., Tan, F.W., and Feng, X.L. 2010. REE geochemistry of marine oil shale from the Changshe Mountain area, northern Tibet, China. International Journal of Coal Geology, **81**(3): 191-199.
Fu, X.G., Wang, J., Zeng, Y.H., Tan, F.W., and He J.L. 2011. Geochemistry and origin of rare earth elements (REEs) in the Shengli River oil shale, northern Tibet, China. Geochemistry, **71**(1): 21-30.
GB/T 14506.1~14-2010. Methods for Chemical Analysis of Silicate Rock. [in Chinese]
GB/T 14506.30-2010. Methods for Chemical Analysis of Silicate Rocks-Part 30: Determination of 44 Elements. [in Chinese]
GB/T 19145. 17-2003. Determination of total organic carbon in sedimentary rock. [in Chinese]
Hou, F.H., Fang, S.X., Dong, Z.X., Zhao, J.S., Lu, S.X., Wu, Y., and Chen, Y.N. 2003. The Developmental Characters of Sedimentary Environments and Lithofacies of Middle Ordovician Majiagou Formation in Ordos Basin. Journal of Sedimentary, **21**(1): 106-112. [in Chinese]
Hou, W. 2010. Application of REE Geochemical Characteristics of Sandstone to Study on Provenance: a case from the Middle Jurassic of Mohe Basin in Northeast China. Acta Sedimentologica Sinica, **28**(2): 285-293. [in Chinese]
Hoyle, J., Elderfield, H., Gledhill, A., and Greaves, M. 1984. The behavior of the rare earth elements during mixing of river and sea waters. Geochimica et Cosmochimca Acta, **48**(1): 143-149.
Johnson, M.R. 2010. Thin section grain size analysis revisited. Sedimentology, **41**(5): 985-999.
Jones, B., and Manning, D. 1994. Comparison of geochemical indices used for the interpretation of palaeo-redox conditions in ancient mudstones. Chemical Geology, **111**(1-4): 111-129.
Kennedy, M.J., Pevear, D.R., and Hill, R.J. 2002. Mineral surface control of organic carbon in black shale. Science, **295**(5555): 657-660.
Kimura, H., and Watanabe, Y. 2001. Oceanic anoxia at the Precambrian-Cambrian boundary. Geology, **29**(11): 995-998.
Kitamura, A. 1998. Glaucony and carbonate grains as indicators of the condensed section: Omma Formation, Japen. Sedimentary Geology, **122**: 151-163.
Lerman, A. 1978. Lakes Chemistry Geology and Physics. Springer-Verlage.
Li, C.R., and Chen, K.Y. 2004. The application of C and O isotope analyse in sediment of Qianjiang saline lake. Natural Gas Geoscience, **15**(3): 320-322. [in Chinese]
Li, D.L., and Zhao, W.W. 2013. Diagenesis and its effect on reservoir properties of Chang 2 oil reservoir set in Longzuigou area of Xiasiwan, Ordos Basin. Lithologic Reservoirs

25(3): 77-81. [In Chinese]
Li, D.L., Li, R.X., Tan, C.Q., Zhao, D., Xue, T., Zhao, B.S, and et al. 2019. Origin of silica, paleoenvrionment, and organic matter enrichment in the Lower Paleozoic Niutitang and Longmaxi formations of the northwestern Upper Yangtze Plate: Significance for hydrocarbon exploration. Marine and Petroleum Geology, **103**: 404-421.
Li, D.L., Li, R.X., Zhu, Z.W., and Xu, F. 2018. Elemental characterstics of lacustrine oil shale and its controlling factors of palaeo-sedimentary environment on oil yield: a case of Chang 7 oil layer of Triassic Yanchang Formation in southern Ordos Basin. Acta Geochimica, **37**: 228-243.
Li, D.L., Li, R.X., Zhu, Z.W., Wu, X.L., Cheng, J.H., and Zhao, B.S. 2017. Origin of organic matter and paleo-sedimentary environment reconstruction of the Triassic oil shale in Tongchuan City, Southern Ordos Basin (China). Fuel, **208**: 223-235.
Li, D.L., Li, R.X., Zhu, Z.W., Wu, X.L., Liu, F.T., Zhao, B.S., and et al. 2017. Elements geochemistry characteristics and paleoenvironment reconstruction on lacustrine oil shale-a case study of "Zhangjiatan Oil Shale" of Triassic Yanchang Formation from the southern Ordos Basin(China). Acta Geochimica, **37**: 1-16.
Li, D.L., Li, R.X., Zhu, Z.W., Wu, X.L., Liu, F.T., Zhao, B.S., and et al. 2017. Rare earth elements geochemistry characteristics and their geological implications of lacustrine oil shale from Chang 7 oil layer in southern Ordos Basin, China. Geological Journal, **52**(1): 119-131.
Li, R.X., and Li, Y.Z. 2008. Tectonic evolution of the western margin of the Ordos Basin(Central China). Russian Geology & Geophysics, **49**(1): 23-27.
Li, W.H., Chen, Q., Li, Z.C., Wang, R.G., Wang, Y., and Ma, Y. 2012. Lithofacies palaeogeography of the Early Paleozoic in Ordos area. Journal of Palaeogeography, **14**(01): 85-100. [in Chinese]
Li, X.H. 1999. U-Pb zircon ages of granites from the southern margin of the Yangtze Block : timing of Neoproterozoic Jinning: Orogeny in SE China and implications for Rodinia Assembly. Precambrian Research, **97**(1): 43-57.
Ling, M.X., Yang, X.Y., Sun, W., Miao, J.Y., and Liu, C.Y. REE/trace element characteristics of sandstone-type uranium deposits in the Ordos Basin. Chinese Journal of Geochemistry, **25**(4): 355-365.
Liu, Q.Y., Chen, M.J., Liu, W.H., Han, P.L., and Guo, Y.R. 2009. Origin of natural gas from the Ordovician paleo-weathering crust and gas-filling model in Jingbian gas field, Ordos basin, China. Journal of Asian Earth Sciences, **35**(1): 0-88.
Liu, X.G. 2015. Cambrian lithofacies paleogeographic characteristics and evolution in the southern margin of Ordos Basin. Petroleum Geology and Engineering, **29**(01): 14-18. [in Chinese]
McLennan S.M. 2001. Relationships between the trace element composition of sedimentary rocks and upper continental crust. Geochemistry Geophysics Geosystems, **2**(4): 203–236.
McLennan, S.M. 1989. Rare earth elements in sedimentary rocks: Influence of provenance and sedimentary processes. Reviews in Mineralogy and Geochemistry, **21**: 169-200.
Miao, L.Y., and Zhu, M.Y. 2014. Trace fossils from the basal Cambrian Xinji Formation in southern Noth China plate and its chronological significance. Acta Palaeontologica Sinica, **53**(3): 274-289. [in Chinese]
Mou, N., and Wu, C.D. 2005. Characteristics and phosphogenesis of phosphorite of the Sinian-Cambiran, west Yangtze area. Acta Scientiarum Naturalium Universitatis Pekinensis, **41**(4): 551-562. [in Chinese]
Ordin, G.S., and Matter, A. 1981. De glauconiarum origine. Sedimentology, **28**: 611-641.
Pan, B., Topper T., Skovsted C., Miao, L.Y., and Li, G.X. 2017. Occurrence of

Microdictyon from the lower Cambrian Xinji Formation along the southern margin of the North China Platform. Journal of Paleontology, **92**(01): 59-70.
Schenau, S.J., Slomp, C.P., and Lange G.J. 2000. Phosphogenesis and active phosphorite formation in sediments from the Arabian Sea oxygen minimum zone. Marine Geology, **169**: 1-20.
Schenau, S.J., Slomp, C.P., and Lange, G.J. 2000. Phosphogenesis and active phosphorite formation in sediments from the Arabian Sea oxygen minimum zone. Marine Geology, **169**(1): 1-20.
Seward, B.L., and Hails, J.R. 2010. An appraisal of the computation of statistical parameters in grain size analysis. Sedimentology, **20**(1): 161-169.
Shemesh, A., Kolodny, Y., and Luz, B. 1983. Oxygen isotope variations in phosphate of biogenic apatites, II. Phosphorite rocks. Earth and Planetary Science Letters, **64**(3): 405-416.
Shi, J.A., Shao, Y., Zhang, S.C., Fu, C.Q., Bai, H.F., Ma, Z.L., and Wu, Z.X. 2009. Lithofacies Paleogeography and Sedimentary Environment in Ordovician Majiagou Formation, Eastern Ordos Basin. Natural Gas Geoscience, **20**(03): 316-324. [in Chinese]
SY/T 5434-2009. Methods for particle size analysis in clastic rocks. [in Chinese]
SY/T 5913-2004. Methods for making rock-section. [in Chinese]
SY/T 6210-1996. X-ray diffraction quantitative analysis methods of the clay minerals and common non-clay minerals in sedimentary rocks. Oil and gas standard of P.R. [in Chinese]
Tamburini, F., Föllmmi, K.B., and Adatte, T. 2003. Sedimentary phosphorus record from the Oman margin: New evidence of high productivity during glacial periods. Paleoceanography, **18**(1).
Tang, D.J., Shi, X.Y., Ma, J.B., and Shi, Q. 2016. Mesoproterozoic glaucony as a potential mineral proxy for shallow chemocline in the Precambrian ocean. Earth Science Frontiers, **23**(6): 219-235. [in Chinese]
Taylor, S., and McLennan, S.M. 1995. The geochemical evolution of the continental crust. Reviews of Geophysics, **33**: 293-301.
Teng, G.E., Liu, W.H., Xu, Y.C., and Chen, J.F. 2005. Correlative study on parameters of inorganic geochemistry and hydrocarbon source rocks formative environment. Advances in Earth Science, **20**(2): 193-200.
Tian, Y., Zhao, X.M., Wang, Z.L., Tu, B., Xie, G.G., and Zeng, B.F. 2014. Geochemical Characteristics and Its Paleoenvironmental Implication of Permian Qixia Formation in Shizhu, Chongqing. Acta Sedimentology Sinica, **32**(6): 1035-1045.
Tribovillard, N., Algeo, T., Lyones, T., and Riboulleau, A. 2006. Trace metals as paleoredox and paleoproductivity proxies-an update. Chemical Geology, **232**(1-2): 12-32.
Vincent, B., Rambeaur, C., Emmanue, L., and Loreau, J. 2006. Sedimentology and trace element geochemistry of shallow-marine carbonates: an approach to paleoenvironmental analysis along the Pagny-sur-Meuse Section (Upper Jurassic, France). Facies, **52**(1): 69-84.
Walker, C.T. 1968. Evaluation of boron as a paleosalinity indicator and its applicationto offshore prospects. AAPG Bulletin, **52**: 751-766.
Walker, C.T., and Price, N.B., 1963. Departure curves for computing paleosalinity from boron in illites and shale. AAPG Bulletin, **47**: 833-841.
Wallin, B. 1989. Origin of the Lower Cambrian phosphatic bed at Vassbo, Sweden. Terra Nova, **1**(3): 274-279.
Wang, C.S., Chen, W.X., and Shan, F.L. 2016. Geochemical Characteristic of the Xungba

579 Formation Sandstones in the Xungba Basin, Tibet, and its Constraints on Provenance
580 and Tectonic Setting. Acta Geologica Sinica, **90**(06): 1195-1207.
581 Wang, X.B., Tang, Y.G., Jiang, Y.F., Xie, P.P., Zhang, S.F., and Chen, Z.J. 2017.
582 Mineralogy and geochemistry of an organic and V-Cr-Mo-U-rich siliceous rock of
583 Late Permian age, western Hubei Province, China. International Journal of Coal
584 Geology, **172**: 19-30.
585 Wang, X.C. 2018. The lithofacies Paleogeography and Depositional System of the
586 Cambrian in the Southwestern Margin of Ordos Basin. Ph.D. thesis, Northwest
587 university, Xi'an, China. [in Chinese]
588 Wang, Z.G., and Yu, X.Y. 1989. Rare-Earth Element Geochemistry. Science Press, Beijing.
589 [in Chinese]
590 Webb, G.E., and Kamber, B.S. 2000. Rare earth elements in Holocene reefal microbialites:
591 a new shallow seawater proxy. Geochimica et Cosmochimica Acta, **64**(9): 1557-1565.
592 Xi, S.L., Li, Z.H., Wang, X., and Zheng, C.B. 2006. Distribution and exploration potential
593 of Ordovician reservoir in Ordos basin. Oil & Gas Geology, **27**(03): 405-412.
594 Xu, L.G., Bernd, L., Zhang, X.G., Zhang, W., and Meng, Q.T. 2014. Trace element
595 distribution in black shales from the Kunyang phosphorite deposit and its geological
596 significances. Acta Petrologica Sinica, **30**(06): 1817-1827. [in Chinese]
597 Xu, Y.H., Zhao, T.P., and Chen, W. 2010. The discovery and geological significance of
598 glauconites from the Paleoproterozoic Xiong'er Group in the Southern Part of the
599 North China Craton. Acta Sedimentologica Sinica, **28**(4): 671-675. [in Chinese]
600 Xu, Z.H., Hu, S.Y., Wang, C.Z., Xu, A.N., and Jiang, Q.C. 2011. Restoration of
601 Paleoclimate and Its Geological Significance: As an example from Upper Triassic
602 Xujiahe Formation in Sichuan Basin. Acta Sedimentologica Sinica, **29**(2): 235-244.
603 Yan, Y., Xia, B., Lin, G., Hu, X.Q., Yan, P., and Zhang F.Q. 2007. Geochemistry of the
604 sedimentary rocks from the Nanxiong Basin, South China and implications for
605 provenance, paleoenvironment and paleoclimate at the K/T boundary. Sedimentary
606 Geology, **197**(1-2): 127-140.
607 Yandoka, B.M.S., Abubakar, M.B., Wan, H.A., Maigari, A.S., Hakimi, M.H., Adgoke,
608 A.K., and et al. 2015. Sedimentology, geochemistry and paleoenvironmental
609 reconstruction of the Cretaceous Yolde formation from Yola Sub-basin, Northern
610 Benue Trough, NE Nigeria. Mar. Petrol. Geol, **67**, 663-677.
611 Yang, Z.Y., Shen, W.Z., and Zheng, L.D. 2009. Elements and Isotopic Geochemistry of
612 Guadalupian-Lopingian Boundary Profile at the Penglaitan Section of Laibin, Guangxi
613 Province , and its Geological Implications. Acta Geologica Sinica, **83**(1): 3-17.
614 Zhang, K. 1981. Cambrian transgression and stratigraphic diachronism in the Ordos region.
615 Scientia Geologica Sinica, **03**: 254-258.
616 Zhang, W.X. 2008. Elemental geochemistry and paleoenvrionment evolution of shell bar
617 section at Qarhan in Qaidam Basin. Quaternary Sciences, **28**(5): 2221-2224.
618 Zhang, Y.S. 2000. Mechanism of Deep Burial Dolomitization of Massive Dolostones in the
619 Middle Majiagou Group of the Ordovician,Ordos Basin. Acta Sedimentologica Sinica,
620 **03**: 424-430.
621 Zhao, B.S., Li, R.X., Wang, X.Z., Wu, X.Y., Wang, N., Qin, X.L., and et al. 2016.
622 Sedimentary Environment and Preservation Conditions of Organic Mteer Analysis of
623 Shanxi Formation Mud Shale in Yanchang Exploration Area, Ordos Basin. Geological
624 Science and Technology Information, **35**(6): 109-117. [in Chinese]
625 Zhu, Y.H., and Ma, L.F. 2008. Division and Correlation of Lower Cambrian and Its
626 Sedimentary Evolution in North China. Geological Review, **54**(06): 731-740. [in
627 Chinese]
628

Table 1. Results of optical microscopy on the Xinji Formation sandstone samples (%).

Sample ID	Lithology	Quartz	Feldspar	Detritus	Carbonate Cement
H25	Argillaceous siltite	55	0	5	40
H22	Siltite	45	1	4	50
H19	Siltite	45	1	9	45
H16	Siltite	75	0	20	5
H13	Argillaceous siltite	85	0	10	5
H11	Fine sandstone	60	0	11	30
H7	Siltite	72	0	13	15
H3	Argillaceous siltite	72	0	13	15
H1	Fine sandstone	68	0	22	10
Average		64.11	0.22	11.89	23.89

Table 2. Results of XRD analysis of the Xinji Formation sandstone samples (%).

Sample ID	Lithology	Quartz	Calcite	Illite	Feldspar	Chlorite	Anhydrite	Hematite
H24	Argillaceous siltite	64.4	7.9	11	13.6	2.3	0.8	/
H22	Siltite	52.7	27.8	9	10	0.5	/	/
H20	Siltite	39.8	29	20.6	7.5	1.1	0.8	0.2
H17	Siltite	58.2	4.5	18.9	17	0.1	0.9	0.4
H15	Argillaceous siltite	73.9	6.2	7.9	12	/	/	/
H13	Argillaceous siltite	59	/	27.6	8.6	1.5	1.3	2
H11	Fine sandstone	49.3	19.6	17	12.6	0.4	/	/
H9	Siltite	54.5	7	24.6	9.9	0.2	1	2.8
H6	Siltite	69	9	11	10.7	/	/	0.3
H4	Siltite	60.2	8.8	19.7	7.6	1.8	/	1.9
H2	Argillaceous siltite	70	6.8	12.6	9.7	0.9	/	/
Average		59.18	12.66	16.35	10.84	0.98	0.96	1.27

Note. "/" represents not analyzed.

Table 3. Grain size parameters for the Xinji Formation sandstone samples (M_Z in Φ).

Sample ID	Lithology	M_Z	σ_1	SK_1	K_G
H25	Argillaceous siltite	4.19	0.38	-0.08	1.57
H24	Argillaceous siltite	4.04	0.44	-0.17	1.84
H22	Siltite	3.92	0.45	0.06	1.64
H19	Siltite	4.14	0.38	0.02	1.63
H18	Siltite	4.03	0.48	0.16	1.62
H16	Siltite	4.46	0.30	-0.62	1.84
H13	Argillaceous siltite	4.28	0.37	-0.22	1.75
H11	Fine sandstone	4.31	0.43	-0.69	2.91
H10	Siltite	3.96	0.49	-0.16	1.56
H7	Siltite	4.23	0.38	-0.24	1.81
H5	Siltite	3.94	0.42	0.24	1.67
H3	Argillaceous siltite	3.92	0.52	-0.08	1.45
H1	Fine sandstone	3.89	0.45	0.13	1.63
Average		4.10	0.42	-0.13	1.76

636 **Table 4. Major element content of the Xinji Formation sandstone samples in %.**

Sample ID	Lithology	TiO_2	MnO	P_2O_5	SiO_2	TFe_2O_3	Al_2O_3	CaO	K_2O	Na_2O	MgO	TOC
H25	Argillaceous siltite	0.38	0.09	0.36	56.51	1.89	7.55	11.82	1.87	0.76	0.65	/
H24	Argillaceous siltite	0.43	0.05	0.37	70.81	2.36	9.1	4	2.17	0.81	0.93	0.46
H23	Argillaceous siltite	0.29	0.1	0.4	47.71	1.58	6.11	17.53	1.65	0.79	0.59	/
H22	Siltite	0.33	0.13	0.37	53.43	2.29	6.64	15.87	1.88	0.63	0.68	/
H21	Argillaceous fine sandstone	0.56	0.09	0.3	64.42	2.28	12.02	4.97	3.11	0.73	0.97	0.63
H20	Siltite	0.49	0.1	0.31	50.11	3.57	11.19	12.9	2.97	0.58	1.3	/
H19	Siltite	0.43	0.13	0.33	39.52	2.42	6.14	21.53	1.68	0.6	0.79	/
H18	Siltite	0.46	0.16	0.41	43.53	3.7	8.75	18.55	2.42	0.39	1.19	/
H17	Siltite	0.44	0.06	0.26	67.18	3.04	12.75	1.93	3.17	0.69	0.93	/
H16	Siltite	0.46	0.05	0.28	70.64	3.17	12.86	1.5	3.3	0.87	0.87	/
H15	Argillaceous siltite	0.29	0.07	0.29	78.06	2.08	7.52	2.01	2.22	0.92	0.49	0.24
H14	Argillaceous siltite	0.38	0.07	0.19	75.11	3.13	10.42	1.64	3.03	0.94	0.77	0.09
H13	Argillaceous siltite	0.63	0.06	0.25	68.24	4.51	13.67	1.49	3.87	0.66	1.19	0.06
H12	Argillaceous siltite	0.24	0.07	0.24	78.19	2.52	7.77	1.76	2.32	0.71	0.57	0.20
H11	Fine sandstone	0.39	0.08	0.26	60.28	3.71	9.01	9.14	2.42	0.78	0.92	/
H10	Siltite	0.37	0.09	0.39	59.27	3.91	8.18	8.86	2.01	0.66	0.78	/
H9	Siltite	0.63	0.05	0.29	64.47	5.36	12.42	2.35	3.47	0.62	1.16	/
H8	Siltite	0.23	0.19	0.24	37.69	4.56	6.34	21.29	1.83	0.62	0.89	/
H7	Siltite	0.56	0.08	0.33	61.34	3.59	10.56	6.48	2.5	0.68	1.05	/
H6	Siltite	0.26	0.14	0.29	69.42	4.18	7.23	4.75	1.97	0.5	0.83	/
H5	Siltite	0.38	0.15	0.34	51.45	3.57	7.17	13.49	1.92	0.46	0.96	/
H4	Siltite	0.42	0.16	0.45	65.58	5.21	9.77	4.13	2.43	0.53	1.01	/
H3	Argillaceous siltite	0.26	0.1	0.37	65.76	3.94	7.99	6.67	2.14	0.69	0.98	0.19
H2	Argillaceous siltite	0.33	0.06	0.41	71.28	3.88	8.06	3.58	1.96	0.52	1.13	0.43
H1	Fine sandstone	0.29	0.07	0.28	69.84	4	9.82	3.17	2.54	0.69	1.08	/
UCC*		0.64	0.10	0.15	66	5.04	15.40	3.59	2.80	3.27	2.48	
Average		0.40	0.10	0.32	61.59	3.38	9.16	8.06	2.43	0.67	0.91	0.29

637 **Note. * Data cited are from McLennan (2001), "/" represents not analyzed, TFe_2O_3 : total iron.**
638

639

Table 5. Element parameters of the Xinji Formation sandstone samples.

Sample ID	lithology	La/Th	La/Yb	Y/Ho	MgO/CaO	U/Th	δU (ppm)	EB (ppm)	Sp (‰)	Sr/Ba
H25	Argillaceous siltite	2.12	10.50	27.13	0.05	0.19	0.72	189.69	11.49	0.45
H24	Argillaceous siltite	1.87	12.73	26.13	0.23	0.15	0.62	369.86	29.09	0.21
H23	Argillaceous siltite	2.36	10.39	27.30	0.03	0.11	0.49	168.04	9.37	0.64
H22	Siltite	2.67	9.90	26.20	0.04	0.14	0.59	171.78	9.74	0.59
H21	Argillaceous fine sandstone	2.12	15.73	26.35	0.20	0.11	0.51	318.73	24.10	0.18
H20	Siltite	2.32	11.72	26.95	0.10	0.11	0.50	174.36	9.99	0.45
H19	Siltite	0.69	6.52	27.83	0.04	0.11	0.48	195.03	12.01	0.87
H18	Siltite	2.42	11.90	26.72	0.06	0.13	0.56	193.12	11.82	0.81
H17	Siltite	2.05	13.33	26.79	0.48	0.12	0.52	214.59	13.92	0.15
H16	Siltite	1.94	12.64	26.29	0.58	0.15	0.63	277.65	20.08	0.16
H15	Argillaceous siltite	2.08	10.04	27.05	0.24	0.11	0.50	225.54	14.99	0.14
H14	Argillaceous siltite	2.13	11.08	27.25	0.47	0.13	0.57	208.71	13.35	0.12
H13	Argillaceous siltite	2.32	15.72	25.98	0.80	0.13	0.56	267.23	19.07	0.13
H12	Argillaceous siltite	2.04	8.76	27.79	0.32	0.12	0.52	208.71	13.35	0.13
H11	Fine sandstone	2.36	8.65	27.23	0.10	0.11	0.51	195.46	12.05	0.33
H10	Siltite	2.18	8.47	26.57	0.09	0.11	0.49	186.19	11.15	0.39
H9	Siltite	1.76	15.60	26.92	0.49	0.11	0.48	257.19	18.08	0.15
H8	Siltite	3.07	7.37	28.47	0.04	0.22	0.81	93.46	2.09	1.12
H7	Siltite	2.19	12.03	26.61	0.16	0.14	0.58	246.40	17.03	0.38
H6	Siltite	2.23	9.11	25.73	0.17	0.16	0.66	176.10	10.16	0.22
H5	Siltite	2.11	10.00	25.93	0.07	0.14	0.58	127.83	5.45	0.49
H4	Siltite	1.82	9.70	24.69	0.24	0.13	0.56	196.93	12.20	0.30
H3	Argillaceous siltite	1.98	6.35	27.11	0.15	0.13	0.57	116.16	4.31	0.37
H2	Argillaceous siltite	1.92	10.61	27.20	0.32	0.11	0.48	170.70	9.63	0.20
H1	Fine sandstone	1.69	7.11	26.84	0.34	0.12	0.54	114.13	4.11	0.15
Average		2.10	10.64	26.76	0.23	0.13	0.56	202.54	12.75	0.37

640

641 **Table 6. Trace element contents of the Xinji Formation sandstone samples in ppm.**

Sample ID	Lithology	Co	Sc	Sr	Zr	Ba	Th	U	B	Hf	Y
H25	Argillaceous siltite	12.01	6.48	100.66	410.4	223	22.05	4.13	59.7	12.26	40.39
H24	Argillaceous siltite	5.05	7.30	60.23	258.9	292	24.21	3.63	131	13.13	31.10
H23	Argillaceous siltite	2.802	6.38	127.26	346.2	200	18.08	1.93	47.7	10.45	37.40
H22	Siltite	4.406	6.99	121.59	309.7	206	15.18	2.12	54.3	9.374	36.94
H21	Argillaceous fine sandstone	6.381	8.29	55.28	513.2	300	26.61	3.02	146	13.02	30.04
H20	Siltite	9.98	11.96	129.62	342.4	285	21.87	2.44	77.5	10.32	36.38
H19	Siltite	5.501	9.17	179.92	530.9	207	30.03	3.18	56.2	12.97	49.81
H18	Siltite	8.421	10.72	186.68	434.6	230	26.76	3.49	74.3	13.	48.89
H17	Siltite	8.793	5.96	41.94	399.3	285	17.07	2	99.5	10.86	22.77
H16	Siltite	5.898	5.22	57.01	133.9	364	14.32	2.21	132	11.16	18.14
H15	Argillaceous siltite	3.662	5.03	48.04	246.6	346	11.43	1.27	81.3	6.83	21.10
H14	Argillaceous siltite	5.27	5.67	48.35	287.6	389	12.02	1.61	94	8.15	18.80
H13	Argillaceous siltite	10.46	8.52	42.04	522.7	320	21.71	2.78	139	14.28	27.02
H12	Argillaceous siltite	3.924	4.83	37.12	211.2	282	9.82	1.14	77.8	5.89	20.01
H11	Fine sandstone	7.646	9.28	76.69	326	230	15.46	1.77	75.2	8.47	38.94
H10	Siltite	6.618	8.54	76	314.8	196	17.76	1.93	62.1	9.42	42.24
H9	Siltite	11.91	8.10	46.27	624.7	311	35.66	3.78	126	14.45	33.11
H8	Siltite	6.776	8.78	200.59	166.9	179	9.88	2.22	28.9	4.91	40.71
H7	Siltite	7.967	9.53	90.91	447.5	237	24.8	3.41	97.1	13.41	38.32
H6	Siltite	6.362	5.97	68.9	218.3	320	12.35	2.03	57.8	6.05	27.53
H5	Siltite	6.34	8.28	125.35	338.7	256	22.57	3.07	41.1	10.7	43.05
H4	Siltite	9.229	7.84	80.8	349.3	267	22.64	2.95	76	10.7	35.55
H3	Argillaceous siltite	8.59	6.38	80.09	201.6	214	12.36	1.64	40.7	5.98	39.04
H2	Argillaceous siltite	11.28	6.78	53.78	303.4	269	19.09	2.03	55.8	8.79	34.55
H1	Fine sandstone	9.966	7.54	50.99	191.9	335	11.84	1.45	45.5	5.63	28.18
UCC*		10	13.6	350	190	550	10.7	2.8	15	5.8	22
Average		7.41	7.58	87.44	337.23	269.72	19.02	2.45	79.06	10.01	33.62

642 **Note. * Data cited are from McLennan (2001).**
643

644
645

Table 7. Trace element enrichment factors for the Xinji Formation sandstone samples.

Sample ID	Lithology	EF(Co)	EF(Sc)	EF(Sr)	EF(Zr)	EF(Ba)	EF(Th)	EF(U)	EF(B)	EF(Hf)	EF(Y)
H25	Argillaceous siltite	2.41	0.96	0.58	4.34	0.81	4.14	2.96	8.00	4.25	3.74
H24	Argillaceous siltite	0.84	0.89	0.29	2.27	0.89	3.77	2.16	14.56	3.77	2.36
H23	Argillaceous siltite	0.70	1.16	0.90	4.52	0.90	4.20	1.71	7.90	4.47	4.22
H22	Siltite	1.01	1.17	0.79	3.72	0.86	3.24	1.73	8.27	3.69	3.84
H21	Argillaceous fine sandstone	0.81	0.77	0.20	3.41	0.69	3.14	1.36	12.28	2.83	1.72
H20	Siltite	1.35	1.19	0.50	2.44	0.70	2.77	1.18	7.00	2.41	2.24
H19	Siltite	1.36	1.67	1.27	6.90	0.93	6.93	2.81	9.26	5.52	5.59
H18	Siltite	1.46	1.37	0.92	3.97	0.72	4.34	2.16	8.59	3.89	3.85
H17	Siltite	1.05	0.52	0.14	2.50	0.62	1.90	0.85	7.89	2.23	1.23
H16	Siltite	0.70	0.45	0.19	0.83	0.78	1.58	0.93	10.38	2.27	0.97
H15	Argillaceous siltite	0.74	0.75	0.28	2.62	1.27	2.15	0.91	10.93	2.38	1.93
H14	Argillaceous siltite	0.77	0.61	0.20	2.20	1.03	1.64	0.84	9.12	2.05	1.24
H13	Argillaceous siltite	1.16	0.70	0.13	3.05	0.65	2.25	1.10	10.28	2.73	1.36
H12	Argillaceous siltite	0.77	0.69	0.21	2.17	1.00	1.79	0.79	10.13	1.98	1.78
H11	Fine sandstone	1.29	1.15	0.37	2.89	0.70	2.43	1.06	8.44	2.46	2.98
H10	Siltite	1.23	1.16	0.40	3.07	0.66	3.08	1.28	7.68	3.01	3.56
H9	Siltite	1.45	0.73	0.16	4.02	0.69	4.07	1.65	10.26	3.04	1.84
H8	Siltite	1.62	1.54	1.37	2.10	0.78	2.21	1.90	4.61	2.03	4.43
H7	Siltite	1.14	1.01	0.37	3.38	0.62	3.33	1.75	9.30	3.32	2.50
H6	Siltite	1.33	0.92	0.41	2.41	1.22	2.42	1.52	8.08	2.19	2.63
H5	Siltite	1.34	1.29	0.76	3.77	0.98	4.46	2.32	5.80	3.90	4.41
H4	Siltite	1.43	0.90	0.36	2.85	0.75	3.29	1.64	7.87	2.86	2.51
H3	Argillaceous siltite	1.63	0.89	0.43	2.01	0.74	2.19	1.11	5.15	1.96	3.37
H2	Argillaceous siltite	2.12	0.94	0.29	3.01	0.92	3.36	1.36	7.00	2.85	2.96
H1	Fine sandstone	1.54	0.86	0.23	1.56	0.94	1.71	0.80	4.69	1.50	1.98
Average		1.25	0.97	0.47	3.04	0.83	3.06	1.52	8.54	2.94	2.76

646 **Note. EF= $(X_{sample}/Al_{sample})/(X_{UCC}/Al_{UCC})$, X means trace element (McLennan 2001; Li et al. 2017).**
647

Table 8. Rare earth element contents of the Xinji Formation sandstone samples in ppm.

Sample ID	Lithology	La	Ce	Pr	Nd	Sm	Eu	Gd	Tb	Dy	Ho	Er	Tm	Yb	Lu
H25	Argillaceous siltite	46.81	98.98	11.80	46.08	8.70	1.45	8.09	1.37	7.65	1.51	4.29	0.69	4.46	0.65
H24	Argillaceous siltite	45.20	113.48	13.58	51.45	8.99	1.50	8.05	1.24	6.38	1.19	3.47	0.54	3.55	0.55
H23	Argillaceous siltite	42.61	89.41	10.78	42.35	7.94	1.44	7.42	1.27	7.07	1.37	3.98	0.61	4.10	0.62
H22	Siltite	40.48	59.51	10.05	38.94	7.34	1.43	7.07	1.23	7.00	1.41	3.99	0.63	4.09	0.62
H21	Argillaceous fine sandstone	56.31	114.83	12.70	48.55	8.54	1.38	7.67	1.16	6.10	1.14	3.44	0.54	3.58	0.55
H20	Siltite	50.76	56.31	11.59	44.16	7.98	1.47	7.66	1.26	7.09	1.35	4.00	0.62	4.33	0.65
H19	Siltite	20.86	96.08	16.61	63.93	11.44	1.89	10.70	1.70	9.48	1.79	5.31	0.83	5.20	0.79
H18	Siltite	64.86	139.99	14.95	56.66	10.39	1.79	10.06	1.69	9.42	1.83	5.28	0.81	5.45	0.81
H17	Siltite	35.05	72.65	7.69	29.13	5.33	0.97	4.82	0.80	4.45	0.85	2.49	0.40	2.63	0.42
H16	Siltite	27.81	56.44	7.41	29.00	5.31	1.08	4.63	0.71	3.69	0.69	2.06	0.33	2.20	0.34
H15	Argillaceous siltite	23.79	50.87	5.95	23.50	4.48	0.94	4.11	0.72	3.99	0.78	2.25	0.35	2.37	0.36
H14	Argillaceous siltite	25.60	59.16	7.23	29.03	5.13	1.00	4.32	0.70	3.70	0.69	2.18	0.35	2.31	0.37
H13	Argillaceous siltite	50.29	109.13	12.75	48.52	8.40	1.40	6.99	1.07	5.41	1.04	3.13	0.48	3.20	0.48
H12	Argillaceous siltite	20.05	65.79	5.22	21.02	4.07	0.82	3.74	0.65	3.74	0.72	2.40	0.34	2.29	0.35
H11	Fine sandstone	36.50	55.77	9.24	37.27	7.13	1.46	7.06	1.20	7.29	1.43	4.11	0.65	4.22	0.61
H10	Siltite	38.63	53.99	9.95	40.39	8.12	1.51	7.89	1.45	8.15	1.59	4.58	0.70	4.56	0.68
H9	Siltite	62.70	129.14	14.35	53.15	9.40	1.44	8.25	1.30	6.62	1.23	3.73	0.57	4.02	0.59
H8	Siltite	30.37	73.34	8.48	34.24	6.79	1.43	6.78	1.25	7.52	1.43	4.37	0.65	4.12	0.66
H7	Siltite	54.24	114.78	13.25	50.35	9.10	1.56	8.39	1.40	7.57	1.44	4.34	0.66	4.51	0.68
H6	Siltite	27.50	66.11	7.80	30.75	5.89	1.17	5.73	0.98	5.53	1.07	3.07	0.47	3.02	0.46
H5	Siltite	47.58	105.09	11.96	46.94	8.79	1.64	8.59	1.48	8.49	1.66	4.94	0.73	4.76	0.74
H4	Siltite	41.24	102.85	10.51	40.86	8.01	1.51	7.81	1.33	7.49	1.44	4.21	0.65	4.25	0.66
H3	Argillaceous siltite	24.50	60.64	7.21	30.65	6.73	1.38	6.66	1.23	7.42	1.44	4.17	0.61	3.86	0.57
H2	Argillaceous siltite	36.59	81.40	9.49	37.95	7.45	1.63	7.20	1.21	6.74	1.27	3.66	0.54	3.45	0.55
H1	Fine sandstone	19.99	48.81	5.86	25.16	5.48	1.20	5.24	0.98	5.59	1.05	3.01	0.45	2.81	0.44
Chondrite*		0.31	0.81	0.12	0.60	0.20	0.07	0.26	0.05	0.32	0.07	0.21	0.03	0.21	0.03

Note. * Data cited are from Taylor and McLennan (1995).

651 **Table 9. Rare earth element parameters for the Xinji Formation sandstone samples.**

Sample ID	Lithology	ΣLREE	ΣHREE	ΣREE	L/H	$(La/Yb)_N$	$(La/Sm)_N$	$(Gd/Yb)_N$
H25	Argillaceous siltite	213.82	28.71	242.53	7.45	7.11	3.47	1.47
H24	Argillaceous siltite	234.20	24.97	259.17	9.38	8.63	3.24	1.83
H23	Argillaceous siltite	194.53	26.44	220.97	7.36	7.04	3.46	1.46
H22	Siltite	157.75	26.04	183.79	6.06	6.70	3.56	1.40
H21	Argillaceous fine sandstone	242.31	24.18	266.49	10.02	10.66	4.25	1.73
H20	Siltite	182.27	26.96	209.23	6.76	7.94	4.10	1.43
H19	Siltite	210.81	35.80	246.61	5.89	2.72	1.18	1.66
H18	Siltite	288.64	35.35	323.99	8.17	8.06	4.03	1.49
H17	Siltite	150.82	16.86	167.68	8.95	9.03	4.24	1.48
H16	Siltite	127.05	14.65	141.70	8.67	8.56	3.38	1.70
H15	Argillaceous siltite	109.53	14.93	124.46	7.34	6.80	3.43	1.40
H14	Argillaceous siltite	127.15	14.62	141.77	8.70	7.51	3.22	1.51
H13	Argillaceous siltite	230.49	21.80	252.29	10.57	10.65	3.86	1.76
H12	Argillaceous siltite	116.97	14.23	131.20	8.22	5.93	3.18	1.32
H11	Fine sandstone	147.37	26.57	173.94	5.55	5.86	3.30	1.35
H10	Siltite	152.59	29.60	182.19	5.16	5.74	3.07	1.40
H9	Siltite	270.18	26.31	296.49	10.27	10.57	4.30	1.66
H8	Siltite	154.65	26.78	181.43	5.77	4.99	2.89	1.33
H7	Siltite	243.28	28.99	272.27	8.39	8.15	3.85	1.50
H6	Siltite	139.22	20.33	159.55	6.85	6.17	3.01	1.53
H5	Siltite	222.00	31.39	253.39	7.07	6.77	3.49	1.46
H4	Siltite	204.98	27.84	232.82	7.36	6.57	3.32	1.48
H3	Argillaceous siltite	131.11	25.96	157.07	5.05	4.30	2.35	1.39
H2	Argillaceous siltite	174.51	24.62	199.13	7.09	7.18	3.17	1.69
H1	Fine sandstone	106.50	19.57	126.07	5.44	4.82	2.35	1.51
Chondrite*		2.11	1.18	3.29	1.79	1.00	1.03	1.00
Average		181.31	24.54	205.85	7.50	7.14	3.35	1.52

652 **Note. ΣLREE= total content of light rare earth elements (ΣLREE= La+Ce+Pr+Nd+Sm+Eu); ΣHREE= total content of heavy rare elements (ΣHREE= Gd+Tb+Dy+Ho+Er+Tm+Yb+Lu);**
653 **ΣREE= total content of rare earth elements (ΣREE= ΣLREE+ΣHREE); L/H= ΣLREE/ΣHREE; N= chondrite-normalized; * Data cited are from Taylor and McLennan (1995).**

Figure Captions

Fig. 1. (a) Map of tectonic zones and phosphate deposits in northern China (Chen 1983). (b) Sedimentary facies map of the Xinji Formation on the southwestern margin of the Ordos Basin (Wang 2017). (c) Regional geological map of the Longxian area.

Fig. 2. Column chart of Cambrian rocks of the south-western margin of the Ordos Basin.

Fig. 3. Photomicrographs of the Xinji Formation sandstone samples: (a) The High carbonate content associated with oolitic biodetritus (sample H18). (b) Corroded quartz grains with carbonate cements and elongate biodetritus (sample H22). (c) Abundant glauconite (sample H7). (d) Abundant oriented hydromica (sample H16). (e) Corroded quartz grains, oriented hydromica, and authigenic glauconite (sample H1). (f) Abundant gluaconite and high carbonate content (sample H3).

Fig. 4. (a) Sandstone triangulation chart for the Xinji Formation sandstone samples (after Li et al. 2013). (b) Triangulation chart of the relative proportions of major elements for the Xinji Formation sandstone samples (after Li et al. 2017).

Fig. 5. UCC-normalized diagram of major elements of the studied samples.

Fig. 6. (a) Enrichment factor diagram of trace elements. (b) Chondrite-normalized distribution patterns of rare earth elements.

Fig. 7. (a) Relationship between ΣREE and SiO_2 for the Xinji Formation sandstone samples. (b) Relationship between ΣREE and P_2O_5 for the Xinji Formation sandstone samples. (c) Relationship between ΣREE and TOC for the Xinji Formation sandstone samples.

Fig. 8. (a) Relationship between TOC and P_2O_5 for the Xinji Formation sandstone samples. (b) Relationship between Al_2O_3 and P_2O_5 for the Xinji Formation sandstone samples.

683

684 Fig. 9. A schematic model with upwelling coastal water and organic matter as a source of the
685 phosphorus (after Wallin 1989).

686

687 Fig.10. (a) Diagrams of provenance (after Floyd and Leveridge 1987). (b) Diagrams of sediments
688 type (after Allègre and Minster 1978).

689

690 Fig. 11. Tectonic background triangulation chart for the Xinji Formation sandstone samples (after
691 Bhatia and Crook 1986).

692

693 Fig. 12. Global climate change curve diagram (after Chen, 2010).

694

695 Fig. 13. (a) Diagrams of P_2O_5 -MgO/CaO for the Xinji Formation sandstone samples. (b)
696 Diagrams of TOC–MgO/CaO for the Xinji Formation sandstone samples.

697

698 Fig. 14. Boron correction and equivalent boron content diagram for the Xinji Formation sandstone
699 samples (after Walker and Price 1963).

700

701 **Fig. 1**

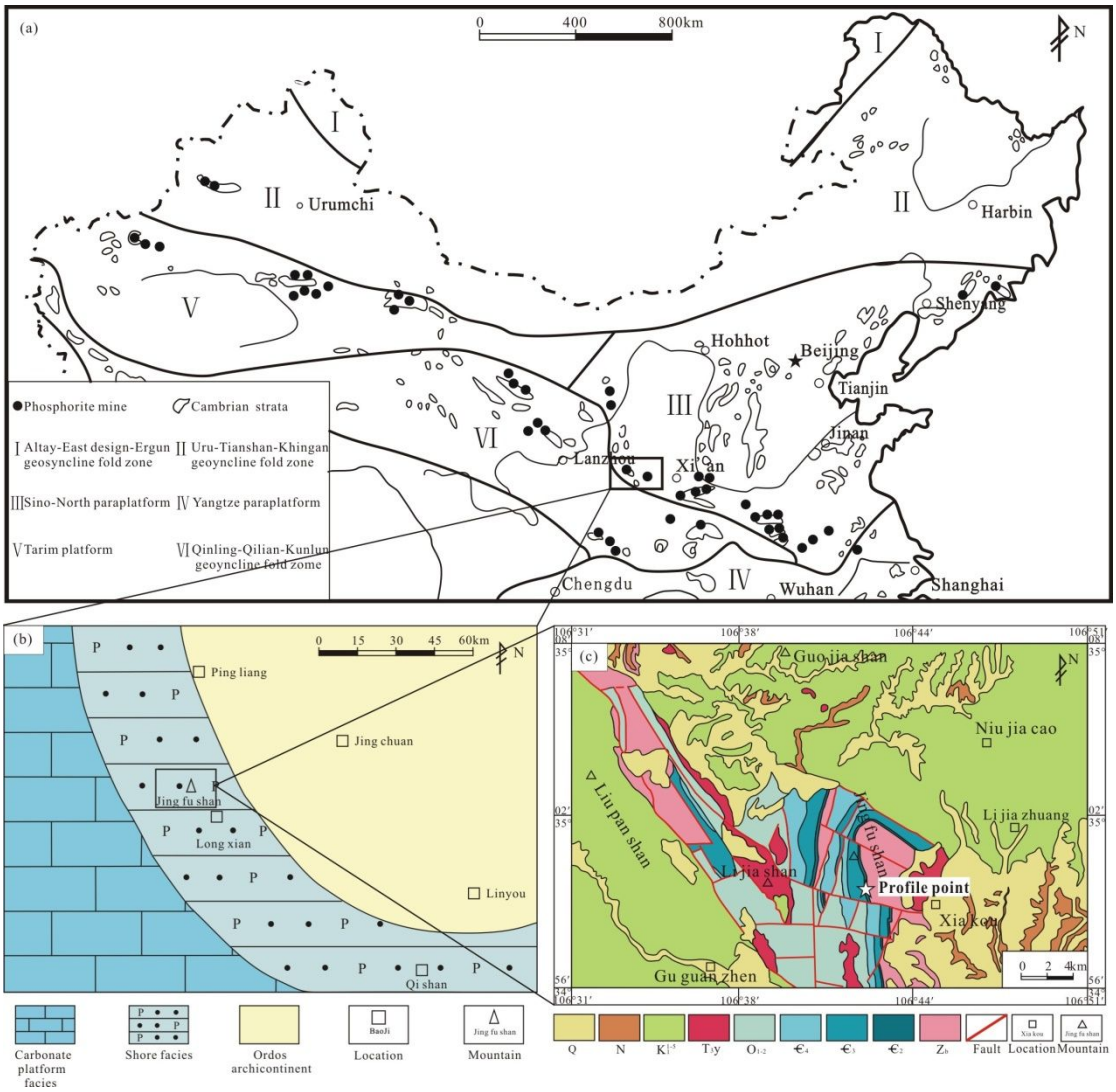

702

703

704

Fig. 2

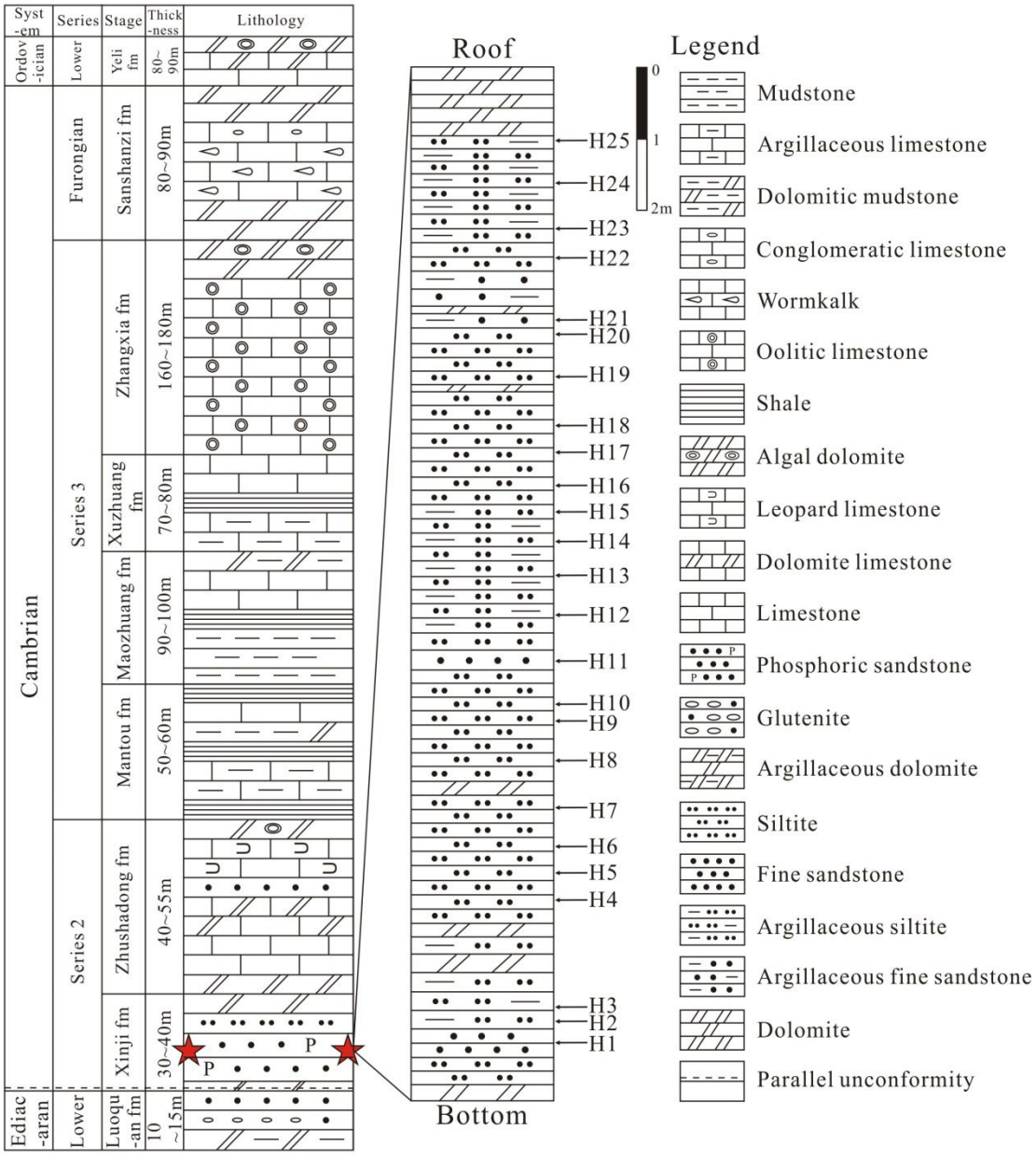

705

706

707 **Fig. 3**

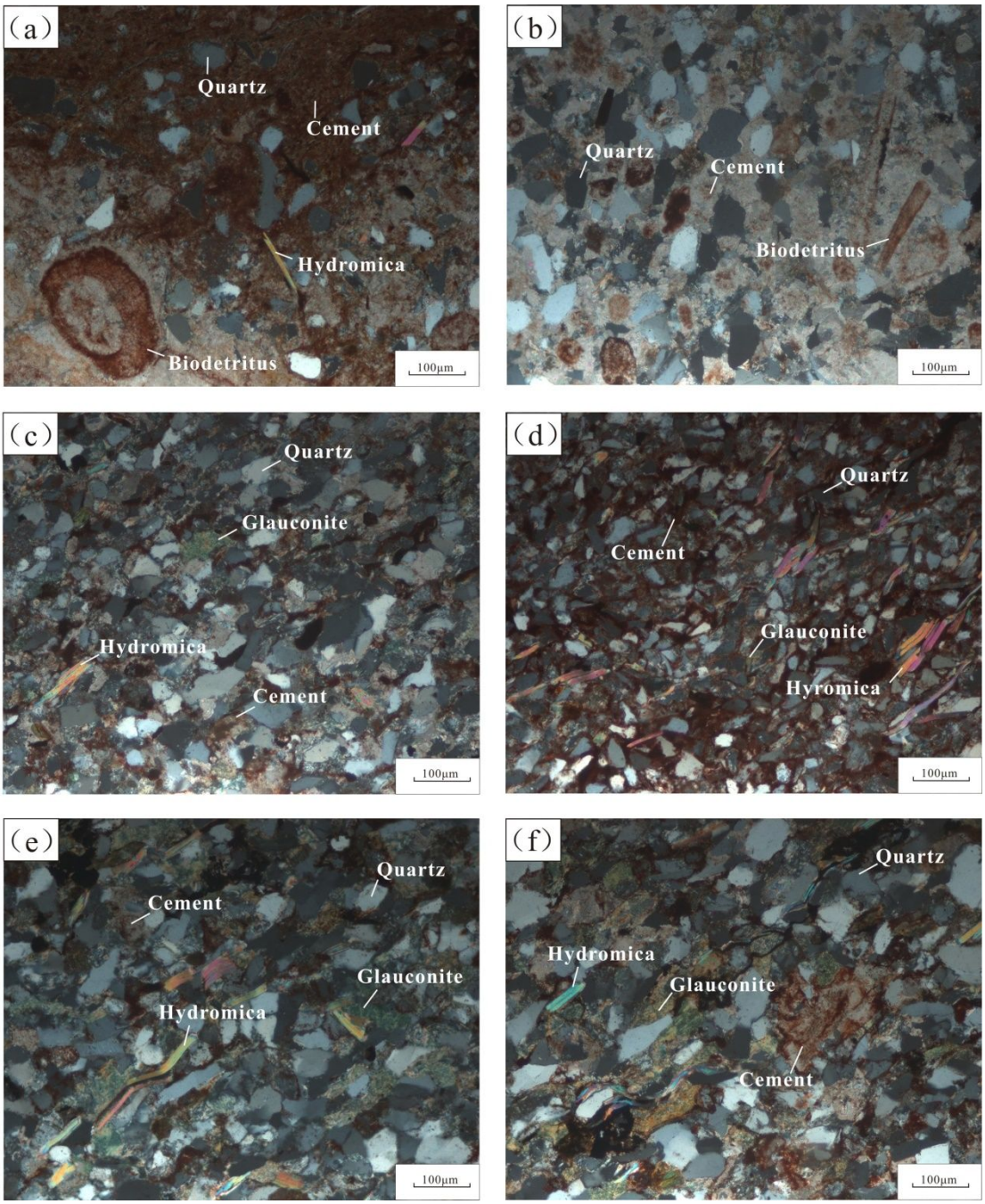

708

709

Fig. 4

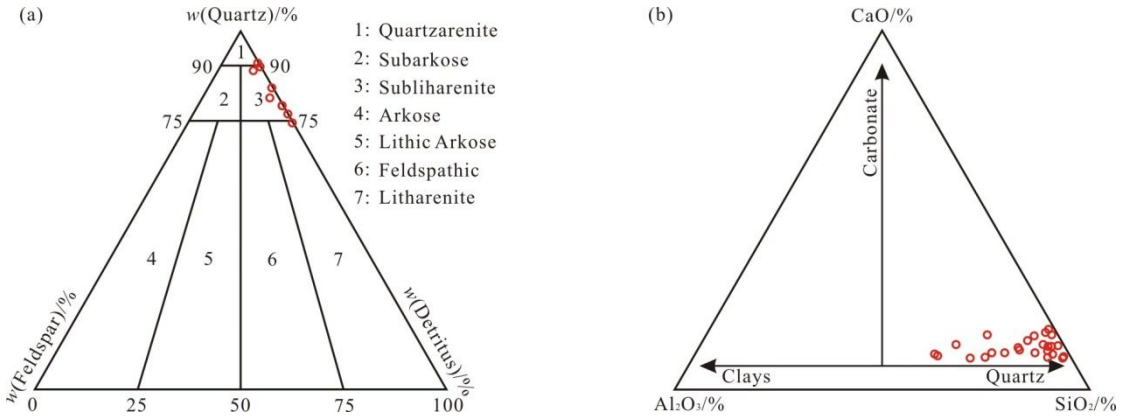

Fig. 5

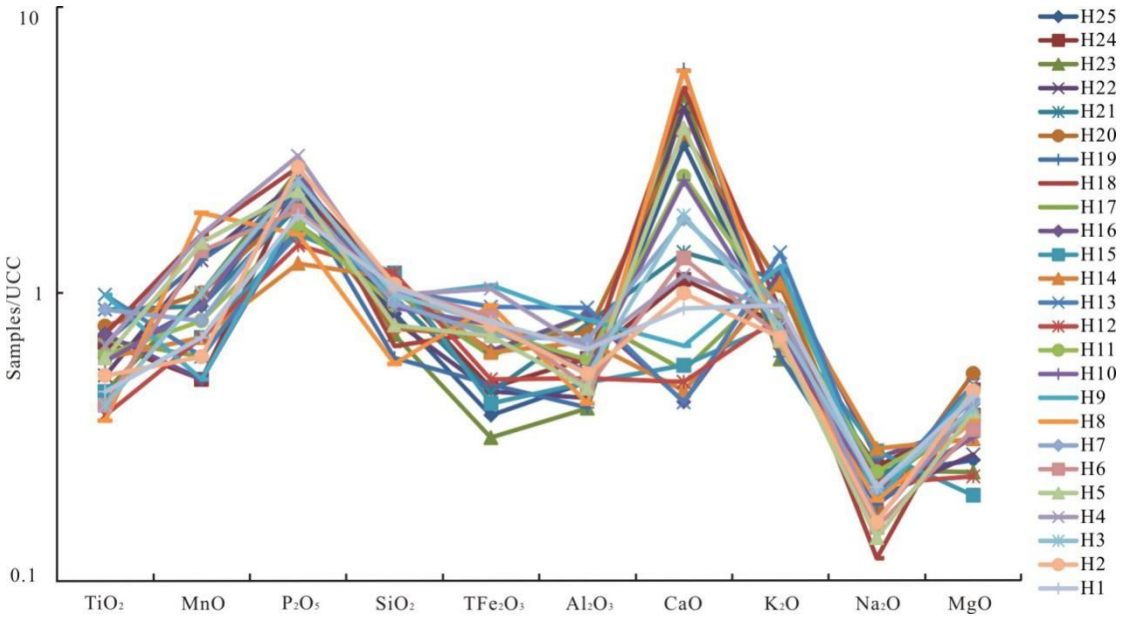

Fig. 6.

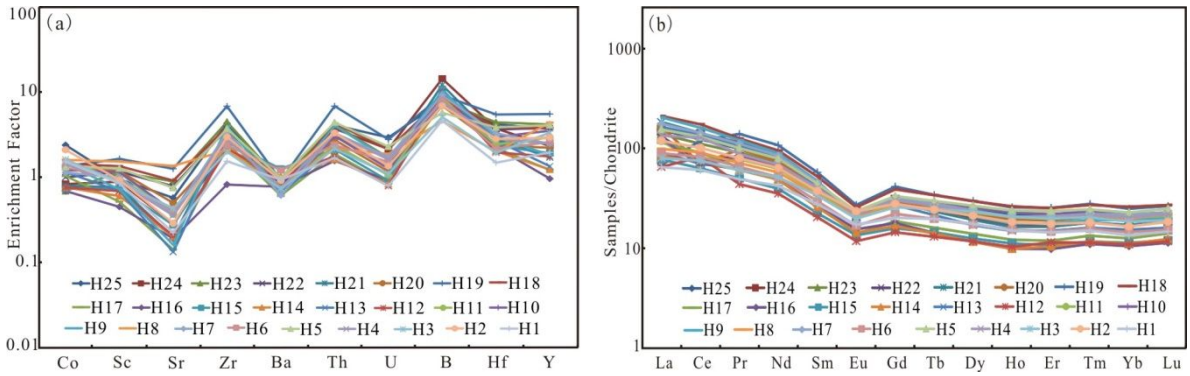

719 **Fig. 7**

720 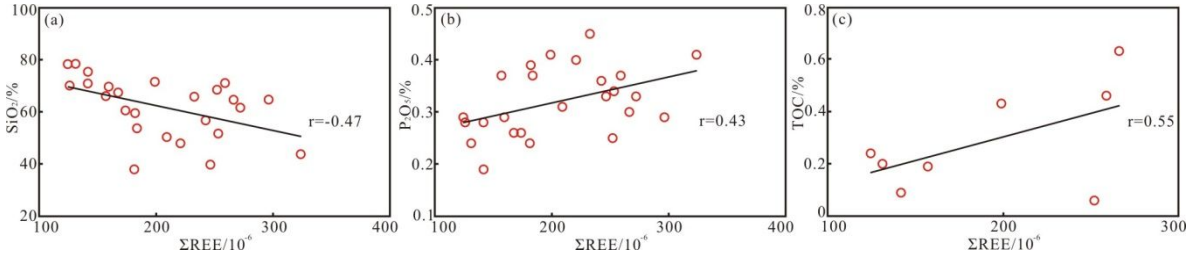

721

722 **Fig. 8**

723 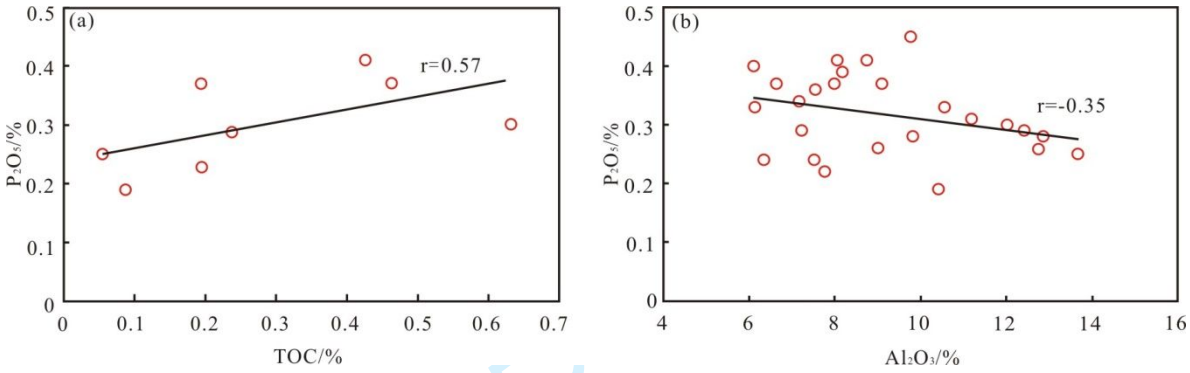

724

725 **Fig. 9**

726 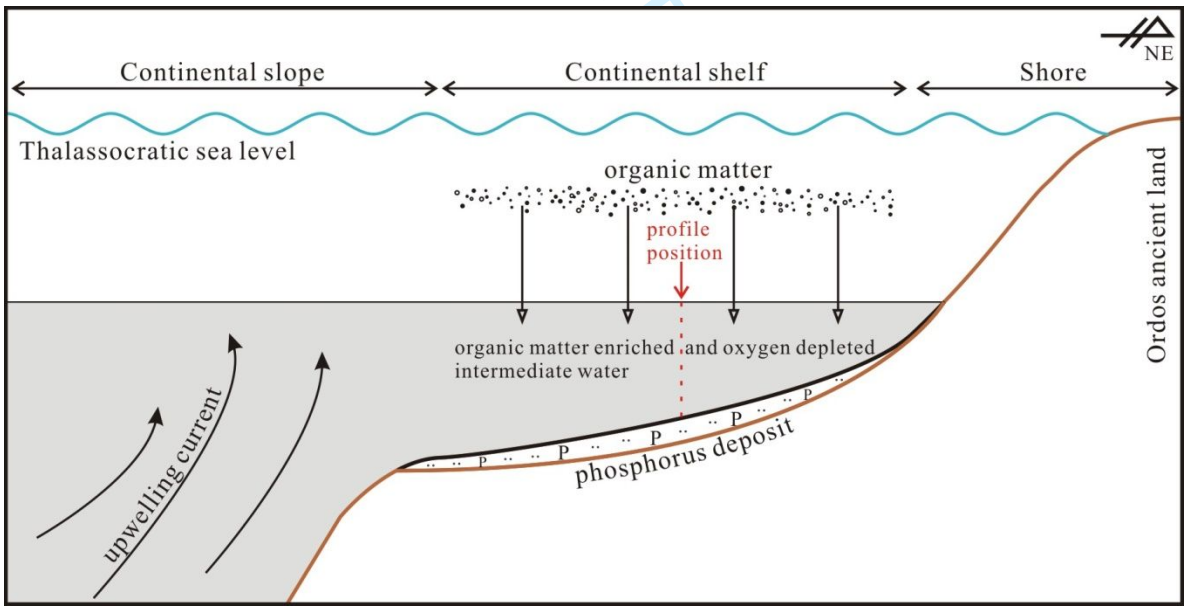

727

Fig.10

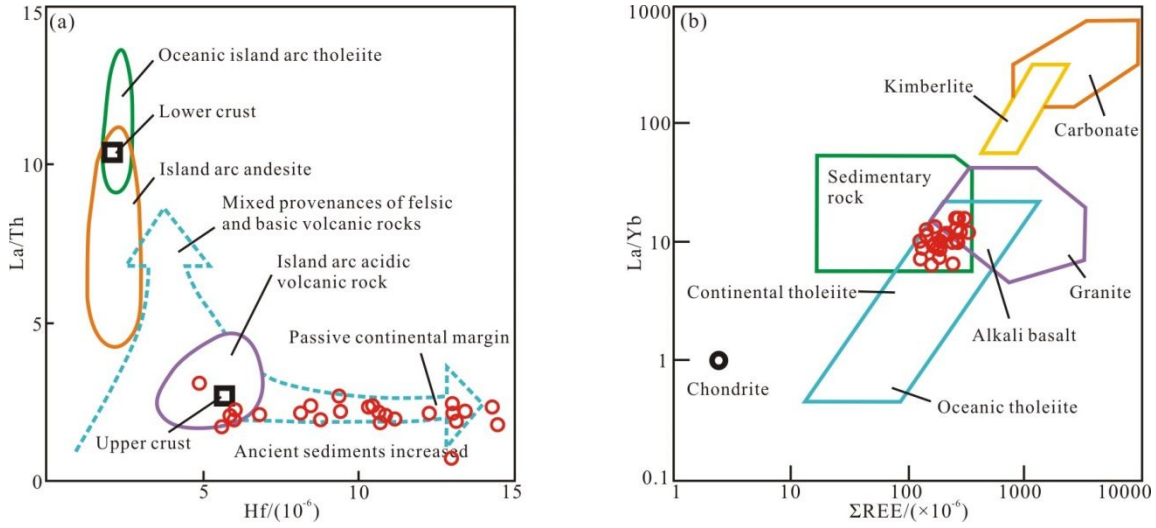

Fig. 11

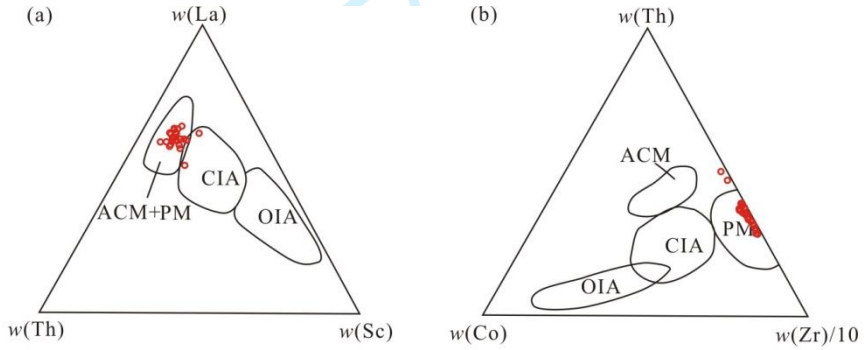

ACM:Active continental margin PM: Passive margin CIA: Continental island arc OIA:Oceanic island arc

Fig. 12

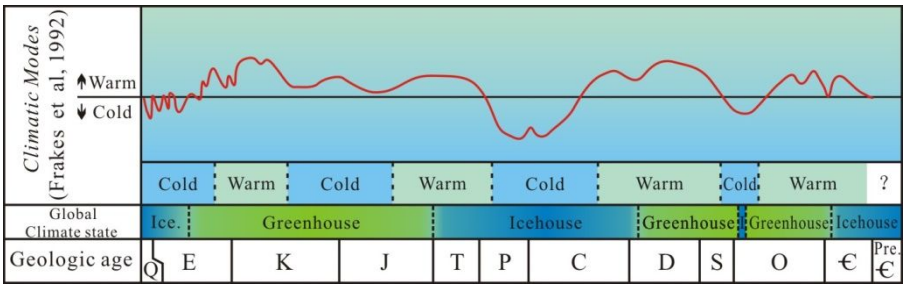

739 **Fig. 13**

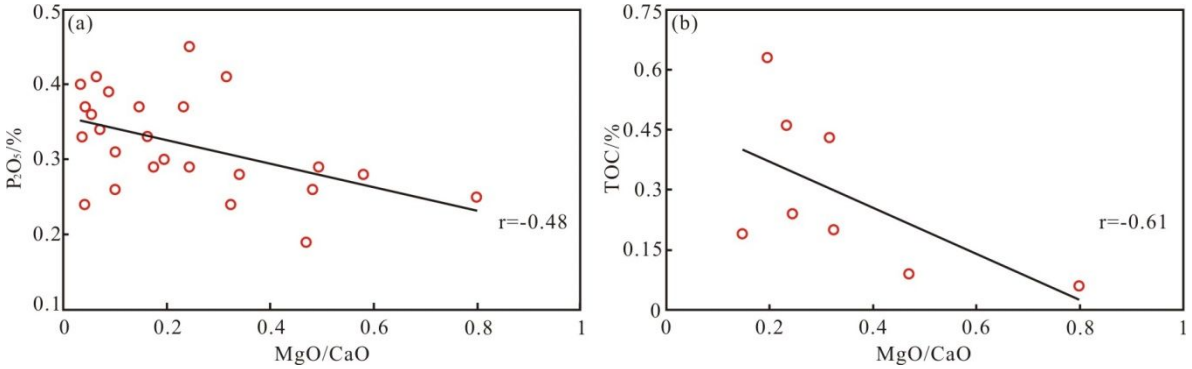

740

741

742 **Fig. 14**

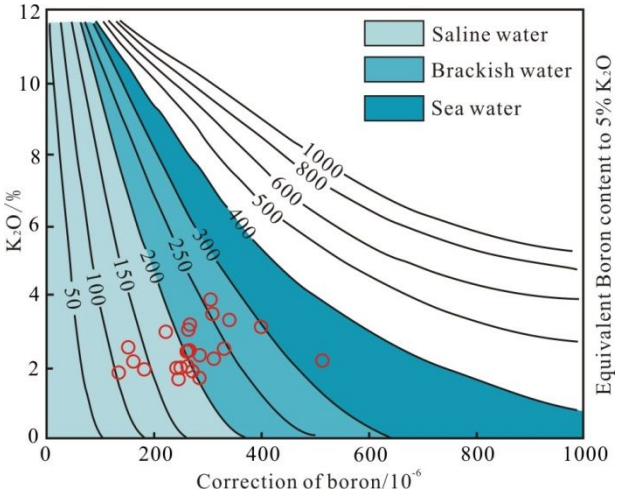

743